In the name of ALLAH the most gracious, the most merciful. I thank ALLAH for helping me during this work.

*I dedicate this to my mother "**Djamila**" who always encourages me in my studies, she is the one who bought me my first laptop which without it my studies would not go this big and my father "**Djamel**" who sent me to the university and supported me mentally and materially and to my brother "**Ferhat**" and my sisters **Keltoum** and **Assia** and her daughters **María** and **Arwa**.*

I also dedicate this work to all my relatives and everyone who knows me.

Messaoud.B

I praise ALLAH for helping me in the achievement of this work.

To people who helped me along the preparation of this project and along all my life, I dedicate this modest work:

To my beloved parents "**Smail** & **Fatima**" for their endless love, support and encouragement .They raised my spirits when necessary and were always there for me. May ALLAH bless them.

To my dear brothers "**Mohamed** & **Salah-Eddine**" and sisters "**Asma** & **Zineb**" whose words of encouragement and push for tenacity ring in my ears every day. They were a real source of inspiration, and to my little nephews **Meriem** , **Belkis** & **Mohamed**.

To all my grand family and my relatives.

My sincere thanks to them all. I will always appreciate all they have done for me.

Abdelatif

Acknowledgments

First of all, we thank ALLAH for giving us faith, strength and patience that we never would have been able to accomplish this work without them. It is a pleasure to thank the many people who made this work possible, but some of them should have a particular mention here.

We would like to thank Dr. CHRIFI Dalila for her excellent guidance from the beginning to the end and for her continuous support which has definitely given an added value to this work. A special thank should go to Professor DERICHE Rachid from INRIA Sophia Antipolis for his effective contribution and work flow monitoring and his PhD student GIRARD Gabriel from Sherbrooke Connectivity Imaging Lab (SCIL) for his active collaboration and responsive Tractometer results, without them this work would not reach that far.

We are thankful to all the researchers of the medical imaging and dMRI community and all the developers of the Open Source Software who helped us in building up our implementation.

We sincerely thank you all.

Abstract

Most of previously published diffusion magnetic resonance imaging reconstruction methods are linked to their own track integration method, some of them use Euler integration others try to improve the integration using the second order and the fourth-order Rang Kutta algorithms. In this work, we have formulated a general, deterministic tractography algorithm (CIERTE), which is a combination of Improved Euler and Range-Kutta fourth-order algorithm, which combine the speed and accuracy at the same time. We have used also tri-linear interpolation, which works with voxel level information about fiber orientations including multiple crossings, and employs a range of stopping criteria as those described in EuDX [1] algorithm and FACT [2]. The purpose of this algorithm is to make tracking accurate and fast at the same time and make it general for all deterministic tracking methods.

Table of content

Acknowledgments III
Abstract IV
Introduction XII
Chapter 1: Introduction to Diffusion MRI 1
1.1 Introduction to Medical Imaging: 2
1.1.1 The basic concept of medical imaging modality: 2
1.1.2 The requirements of medical imaging system: 3
1.1.3 Common Imaging Modalities: 3
1.1.4 Multi-disciplinary in medical imaging: 3
1.1.5 Medical Imaging over time: 4
1.1.6 Magnetic 4
1.1.7 MRI Imaging: 5
1.2 Introduction to Diffusion MRI: 6
1.2.1 Bownian motion and Fick's laws: 6
1.2.2 How to measure diffusion with MRI? 9
1.3 Summary: 12
Chapter 2: From dMRI Reconstruction Models to Brain Tractography 14
2.1 Diffusion MRI techniques: 15
2.1.1 Diffusion-weighted imaging (DWI): 15
2.1.2 Diffusion Tensor Imaging (DTI): 16
2.1.4 Diffusion Spectrum Imaging (DSI): 22
2.1.3 Q-ball imaging (QBI): 23
2.1.4 Constrained Spherical Deconvolution (CSD): 25
2.1.5 Peaks from Models: 26
2.2 Tractography Methods: 27
2.2.1 Local Approach: 27
2.2.2 Global Approach: 29
2.2.3 Simulated approach: 31
2.3 Summary: 31
Chapter 3: CIERTE A Proposed Deterministic Tractography Algorithm 32
3.1 Introduction: 33
3.2 CIERTE Algorithm: 33

3.3 Experimental Results: 45
3.4 Effects of changing the step size: 51
3.5 Summary: 53
Chapter 4: CIERTE Evaluation Using Tractometer 54
4.1 Introduction: 55
4.2 The Tractometer Evaluation System 56
4.3 Phantom Data preparation: 58
4.3.1 Phantom Data : 58
4.3.2 Tractography evaluation pipeline: 59
4.4 Tractometer Results: 60
4.4.1 Deterministic Results: 60
4.4.2 Probabilistic Results: 62
4.5 Visualization of phantom results: 63
4.6 Summary: 64
CONCLUSION: XIII
References : XIV

List of Tables:

Table 3.1: Error calculation in three different tracks.....39

Table 4.2: Comparison between CIERTE-Det , Dipy-Eudx and Dipy-Mx algorithms using three different SNR 10,20,30 and step size 0.2,0.3,0.4 and NPV 50 and 20.....60

Table 4.3 :Comparison between CIERTE-Prob and Maximum direction getter(Dipy-Prob) algorithms using step size (SS) 0.2,0.3,0.4 and NPV 50 and 20 62

List of Figures :

Figure 1.1: medical imaging system diagram.....2
Figure 1.2: Sciences involved in medical imaging. 4
Figure 1.3:medical imaging evolving over time, x-ray, CT, Ultra sound and MRI 4
Figure 1.4: a typical 1.5 T MRI System 5
Figure 1.5 :application of MRI in many fields dMRI, fMRI, heart and muscles 5
Figure 1.6:application of MRI in Diffusion Weighted images (DWI) and Diffusion Tensor images (DTI).....6
Figure 1.7:Random paths of pollen grains molecules in water 7
Figure 1.8:Random paths of pollen grains molecules in water. 7
Figure 1.9: (a) PDF in restricted diffusion (isotropic), (b) Single orientation (looks like cigar shaped) PDF and (c) Various orientations.....9
Figure 1.10: The variantion of S with respect to b (inversely proportional). 10
Figure 1.11: PDF space and q-space are a Fourier pair.....11
Figure 1.12: Full diffusion PDF in 2D (a) Diffusion PDF along two arbitrary directions (b) the length of the radius of ODF is the sum of areas under the curve (c).....12
Figure 2.1: Diffusion distance versus sequare root of diffusion time.....15
Figure 2.2: Diffusion-weighted MR imaging corresponds to one point in q-space. 15
Figure 2.3: Tensor representation as ellipsoid.....16
Figure 2.4: Different forms of diffusion tensor representation based on the isotropy. 17
Figure 2.5: Six points in q-space with q≠0 (DWI) + one point with q=0 are required in DTI. 17
Figure 2.6: An intensity image at each voxel. **Figure 2.7**: A tensor peak map at each voxel.....18
Figure 2.8: Tensor visualization at each matrix component.....19
Figure 2.9 The tensor models(DTI) (A) and its corresponding ODF representation (B) and Peaks-from-model segments(it will be covered in this chapter)(C) to be used in showing tracts (fibers) using tractography(it will be covered in this chapter)(D) for a region in the CC (Corpus Callosum). 21
Figure 2.10: The number of fibers may be greater than one in each voxel. 21
Figure 2.11: Diffusion in an environment with multiple fiber populations the true diffusion PDF (b) and its isoprobability surface (c) are able to characterize the underlying fiber populations (a), the diffusion tensor model can not characterize the real fiber crossing (d)..22
Figure 2.12: DSI requires about 515 DW Images. 23

Figure 2.13 : q-space requires more than 60 DWI.....24
Figure 2.14 : HARDI q-space sampling 24
Figure 2.15: comparing between different methods of reconstruction (CSD,DTI and Q-ball). 26
Figure 2.16 : CSD models as shown using our software. 26
Figure 2.17 : The peaks obtained using our software. 26
Figure 2.18:The FACT method for fiber tracking. 27
Figure 3.1: In every voxel centre (black dot) there are one or more vectors. These vectors represent peaks where their length is equal to their anisotropy value and the direction is equal to the direction of the peake.g. calculated from a given ODF. Eudx as well as CIERTE can track multiple peaks starting from a single seed point (star) if their anisotropy values are higher than a threshold. In that way we can track from the same seed towards different directions and support tracking in crossing areas as it is shown here 40
Figure 3.2: tractography using CIERTE algorithm for CSD, DTI and QBI using low Anisotropy threshold of 0.88, 0.2 and 0.2 respectively 46
Figure 3.3: The effect of changing the low Anisotropy threshold in the CSD model using 0.2, 0.7 and 0.88 respectively 47
Figure 3.4: Multiple crossing fibers Using CSD model as a reconstruction technique.....48
Figure 3.5: Tractography of the brain using 500000 seed points and 0.5 step size with CSD model by tacking the low anisotropy threshold to be 0.88 using CIERTE algorithm.....49
Figure 3.6 :an overview of our DIVIZ software when visualizing tractography. 49
Figure3.7 :Deterministic tractography visualized using DIVIZ from different view angels 50
Figure 3.8: The effect of changing the step size on the fiber tracks 51
Figure 3.9: The tracking point error values/numbers relation with different step-sizes.....51
Figure 3.10: The number of erroneous tracking points in affected streamlines for different step-sizes (0.2, 0.3, 0.4 and 0.5). 52
Figure 3.11: memory usage (RAM) versus step-size. 53
Figure 4.1. Example of a tractography pipeline output and the resulting valid connections filtered by the ROIs 57
Figure 4.2 :Invalid Connections (IC) between 2 ROIs of gray matter on the FiberCup and the real data analogies.....57
Figure 4.3 :No connections (NC) due to many collisions with the tracking mask or angular constraints not met, both causing the tracking process to finish prematurely on the FiberCup and the real data analogies.....57

Figure 4.4:FiberCup mimicking a coronal slice of the brain with typical short 'U' fibers (bundle 4), larger 'U' fibers mimicking the corpus callosum (bundle 1), left-to-right hemisphere commissural projections (bundle 3) and fanning bundles mimicking the corticospinal tract (bundles 2, 5, 6 and7).....58
Figure 4.5:tractography Evaluation pipeline 59
Figure 4.6 : some DWI images (axial #19,coronal #22 and sagittal #31) used for tractography evaluation and their Fiber orientation direction images (FOD) 63
Figure 4.7:visualization of CIERTE tractography results of the phantom data used to evaluate the tractometer results ,images A,B,C,D,E,F are phantom tractography visualization from different points of view ,images E and F illustrate some crossing fibers. 64

Nomenclatures:

3D FT	Three dimensional Fourier Transform
3D IFT	Three dimensional Inverse Fourier Transform
ABC	Average Bundle Coverage
ADC	Apparent Diffusion Coefficient
CIERTE	Combination of Improved Euler and Range-Kutta using Tracking Error
CSA	Constant Solid Angle
CSD	Constrainted Spherical Deconvolution
CSR	Connection Sum Ratio
CT	Computed Tomography
dMRI	Diffusion Magnetic Resonance Imaging
DSI	Diffusion Spectrum Imaging
DTI	Diffusion Tensor Images
DWI	Diffusion Weighted Images
EuDX	Euler Delta Crossing
FA	Fanctional Anisotropy
FACT	Fiber Assignment by Continuous Tracking
fODF	functional Orientation Distribution Function
GFA	General Fraction Anisotropy
HARDI	High Angular Resolution Diffusion Imaging
IB	Invalid Bundles
IC	Invalid Connections
MRI	Magnetic Resonance Imaging
NC	No Connections
NMR	Nuclear Magnetic Resonance
ODF	Orientation Distribution Function
PDF	Probability Density Function
QBI	Q-ball Imaging
RK4	Range-Kutta fourth order
ROI	Region of Interest
SD	Spherical Deconvolution
SH	Spherical Harmonic
SNR	Signal to Noise Ration
SS	Step Size
TEND	Tensor Deflection Tractography
VB	Valid Bundles
VC	Valid Connections
VCCR	Valid Connection to Connection Ratio
WM	White Matter

Introduction

Diffusion magnetic resonance imaging short for dMRI combines information about the local microstructure of the white matter across different voxels; these information can be used to visualize large-scale organization of the brain. Many researchers have been using various algorithms to track along the fibers populations to make inference about axonal connections between different parts of the gray matter. Fiber tractography methods provide tools for piecing together the local WM orientations to infer large-scale connectivity patterns between different brain regions. Diffusion MRI based fiber tractography is unique in its ability to delineate the WM fiber bundles non-invasively and in-vivo [3].

Tractography algorithms often depend strictly on the underlying voxel model these lead other researchers to apply their own reconstruction methods. Fiber Tractography algorithms can be classified largely into two major categories deterministic and probabilistic algorithms.

Our work is divided into four chapters; the first chapter gives you a general idea about scientific basis of Nuclear Magnetic Resonance (NMR) that dMRI is based on, from the random motion in fluids and molecular diffusion to its mathematical description and how it is measured in MR scanners. This would be a brief introduction to the subject, which will be easier to understand by having such a background. In the second chapter, we will discuss the reconstruction models that are known nowadays for their simplicity or performance as well as the factors of consideration on each one then we will see the different global and local approach methods used for tractography in general.

Our contribution in this work is represented in a new proposed purely deterministic tractography algorithm that we have implemented to be fast and accurate hoping that our contribution will be a plus to the deterministic tractography algorithm family. Most importantly it can have as input model-based or model-free reconstruction algorithms of most known algorithms which may increase its flexibility, we call our algorithm "CIERTE" Combined Improved Euler Range-Kutta using Tracking Error.

The third chapter contains the theory and mathematics involved in implementing the CIERTE algorithm as well as the procedure and criteria that affect the flow of the algorithm while working, after that we visualize the tractography results of our proposed algorithm when applied to a real data of a human brain for different criteria on our software DIVIZ, which is a software we developed using Python programming language and the Diffusion

imaging library Dipy. This work is a result of three years of continuous study and development in dMRI field.

CIERTE has a lot of similarity with the EuDX algorithm which can deal with any number of crossing fibers as long as the reconstruction algorithm supports them. The only difference between the EuDX and CIERTE is the method of integrating through the streamlines which is using Improved Euler with a combinational approach of the fourth-order Range-Kutta algorithm; we attained this approach by calculating a tracking error between the improved Euler and the Euler approximations.

To give our proposed algorithm credibility, some statistical study with other deterministic algorithms should be performed, this is done in the fourth chapter where we compared CIERTE algorithm to two state-of-the-art algorithms Eudx and Dipy-MX by comparing their results while varying the different criteria and input parameters. This will give us a reliable ground to evaluate CIERTE algorithm.

"If the brain would be so simple that we could understand it, we would be so simple that we could not understand it"

-Emerson Pugh

Introduction to Diffusion MRI

In this chapter, we are going to introduce the medical imaging in general then we will branch out to the diffusion Magnetic Resonance Imaging (dMRI), the mathematical development behind its evolution as well as the physical and chemical principles and theories that dMRI stands on in order to give you a solid background to understand the more complicated concepts explained in the later chapters.

1.1 Introduction to Medical Imaging:

Before 1895 the only possible way to look inside the body is to open it, in 1895 X-ray was discovered, which revolutionized diagnostic medicine, it was the first time to see internal anatomy. Today with medical imaging, one can visualize the functionalities of many parts of the body, which allows surgeons to locate brain tumors and visualize the neurons around it before doing surgery.

1.1.1 The basic concept of medical imaging modality:

The concept of medical imaging based on the conservation of energy law and the properties of the human as well as its reaction to external sources of energy. It uses the interaction of the body with such sources to visualize its internal structure without surgery by emitting some kind of energy to the body, which absorb it and generate another kind of energy, this last will be detected by a sensor or a detector, this energy could be Electromagnetic, Sound Wave, Nuclear or magnetic. The detector will serve the signal to an imaging system, that will translate the signal to an image from the information encoded in the signal. The medical imaging concept is shown in Figure 1.1.

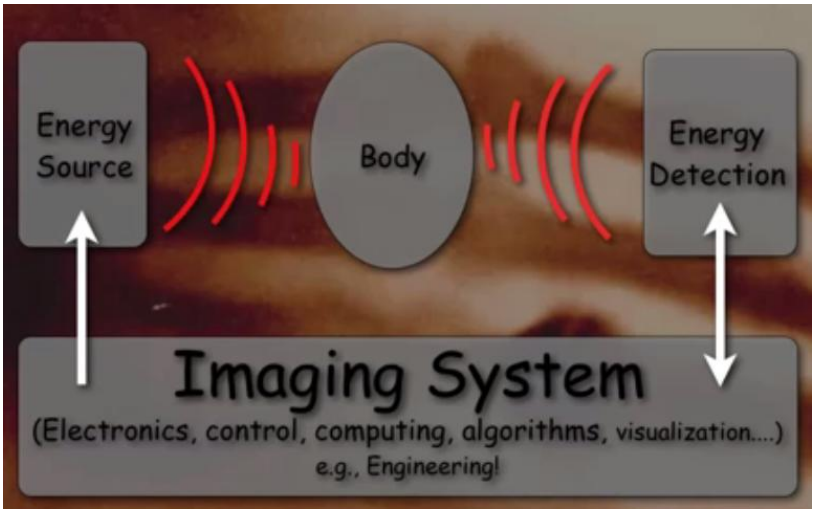

Figure 1.1: *Medical imaging system diagram*

.

1.1.2 The requirements of medical imaging system:

Medical imaging system need to be more sensitive because the sensitivity has a crucial role on the quality of the acquired signal. To be so, many medical imaging systems are built to be specific and perform a single task which may leave us no option to perform several modalities in order to have a good diagnostic. These systems also need to be fast and safe, inexpensive and easy to use.

1.1.3 Common Imaging Modalities:

Since we cannot satisfy all the requirements into one machine many modalities have been used in today medical imaging some of them are shown below:

- Projection X-Ray (Electromagnetic)
- Computed Tomography (Electromagnetic)
- Ultra Sound (Sound Wave)
- Positron Emission Tomography(Nuclear)
- Single-Photon Emission Tomography (Nuclear)
- Magnetic Resonance Imaging(magnetic)

1.1.4 Multi-disciplinary in medical imaging:

The field of medical imaging is really a multi-disciplinary subject many sciences are involved into making a good diagnostic in this work we are interested in the engineering part of medical imaging.

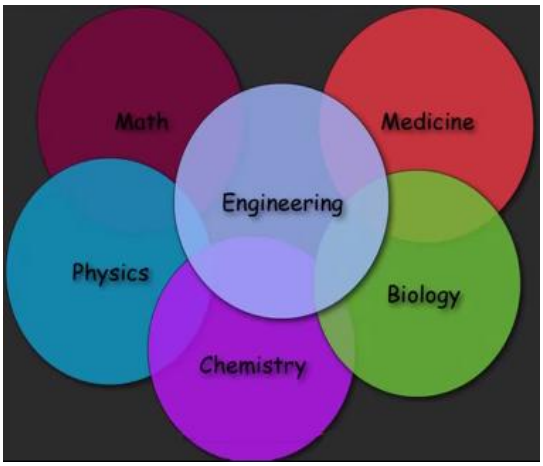

Figure 1.2: *Sciences involved in medical imaging.*

1.1.5 Medical Imaging over time:

Medical imaging is evolving over time as we can see in figure 1.3 many changes happen started from 1895, with x-ray and today's MRI and CT scanners are better.

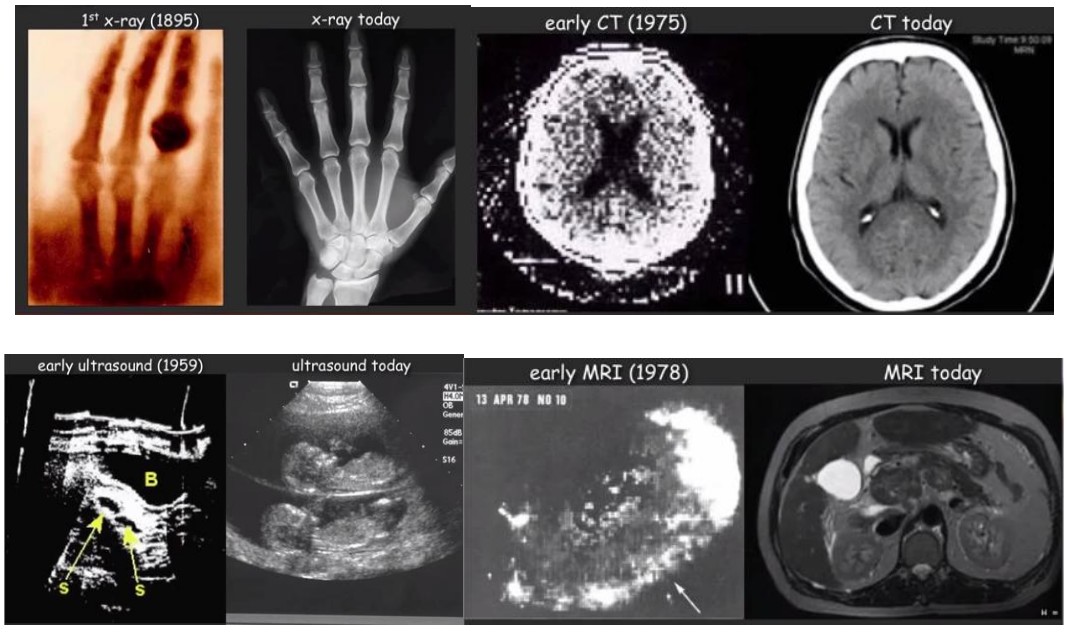

Figure 1.3: *Medical imaging evolving over time, x-ray, CT, Ultra sound and MRI*

1.1.6 Magnetic Resonance Imaging History

Magnetic resonance imaging (MRI) has revolutionized medicine, since 1946 when Felix Bloch (Stanford) and Edward Purcell (Harvard) independently discovered Nuclear Magnetic Resonance (NMR). They got the Nobel Prize (Physics) in 1952. Raymond Damadian showed

changes in MR parameters (T1 and T2) in cancer in 1971.People started thinking about medical NMR applications. The Invention of Computed Tomography by Hounsfield and Cormack in 1972 get them a Nobel Prize (Medicine) in 1979.

Scientists start describing CT and MRI in a similar way, Lauterbur in 1973, proposed key concepts related to chemistry in 1975, which credits him with a Nobel Prize (chemistry) 1991. In 1982, clinical MRI begins to be used widely in disease diagnosis.

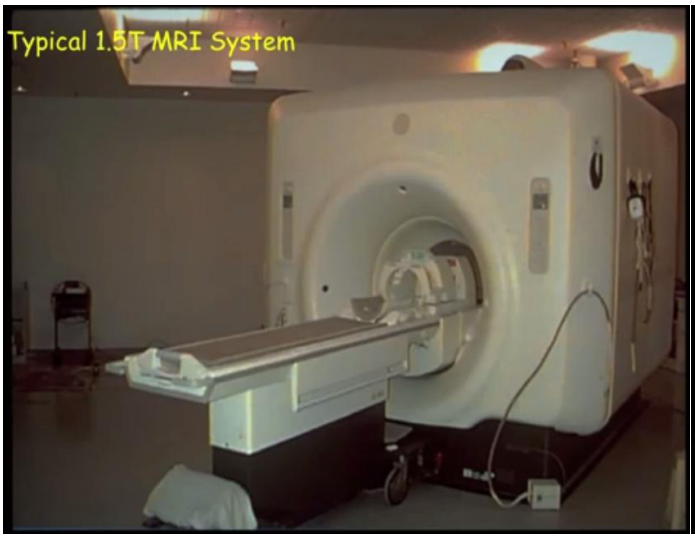

Figure 1.4*: A typical 1.5 T MRI System*

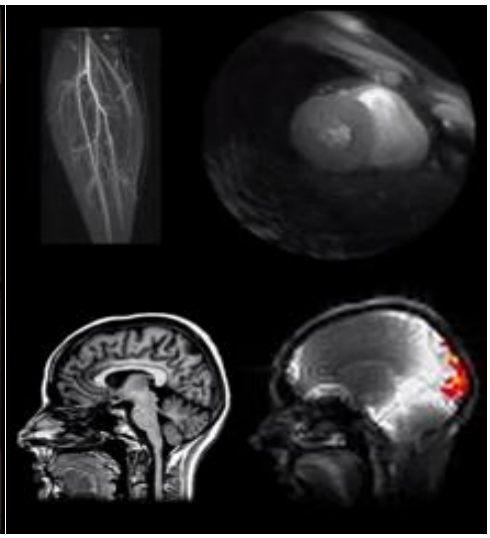

Figure 1.5 :*Application of MRI in many fields dMRI, fMRI, heart and muscles*

1.1.7 MRI Imaging:

Magnetic resonance imaging (MRI) has many applications in the field of medical imaging some of them are:

- Directly visualizes soft tissue in 3D.
- Wide range of contrast mechanisms.
- Tissue character (solid, soft, liquid, fat …).
- Diffusion.
- Temperature.
- Flow, velocity.
- Oxygen Saturation.

For our study, we are interested in diffusion MRI (dMRI) which will be explained later.

The applications of MRI to different fields are shown in Figure 1.5.

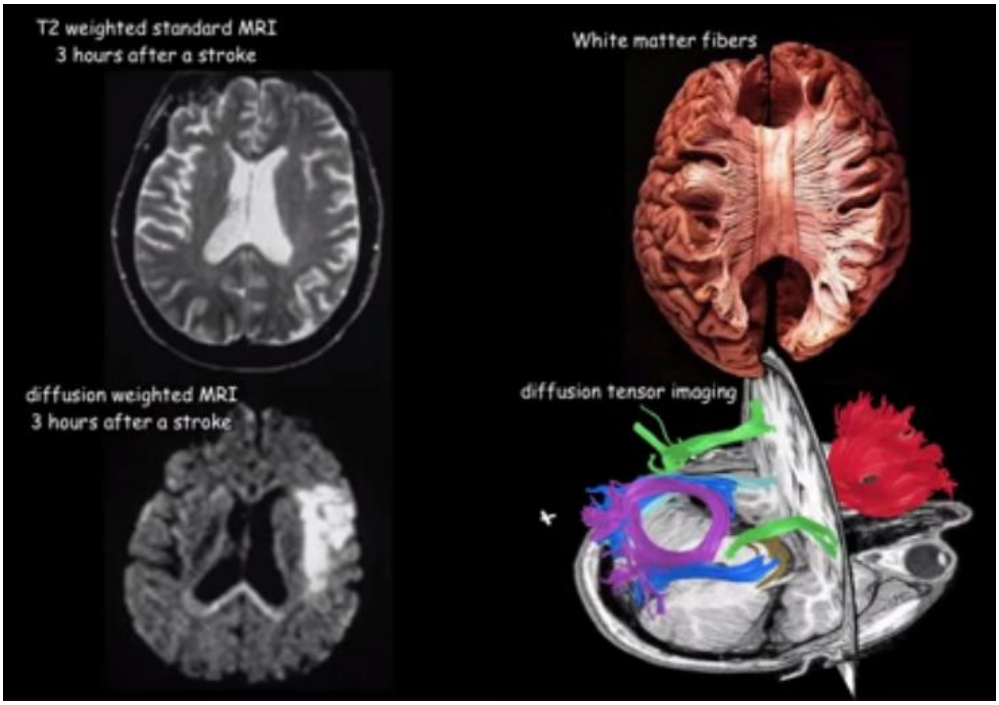

***Figure 1.6**:Application of MRI in Diffusion Weighted images (DWI) and Diffusion Tensor images (DTI).*

As we can see in figure 1.6 the application of MRI in the field of Diffusion, which will be later explained in details.

1.2 Introduction to Diffusion MRI:

1.2.1 Brownian motion and Fick's laws:

The botanist Robert Brown made an experiment in 1827 to observe the behavior of pollen grains when put in water. Looking through a microscope, the particles were moving through the water randomly but he was not able to determine the mechanisms that caused this motion [4].

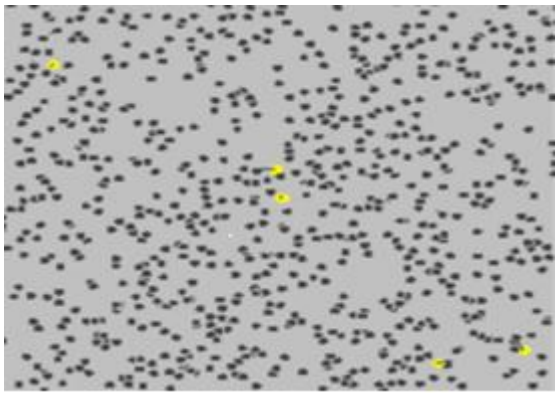

Figure 1.7: *Random paths of pollen grains molecules in water*

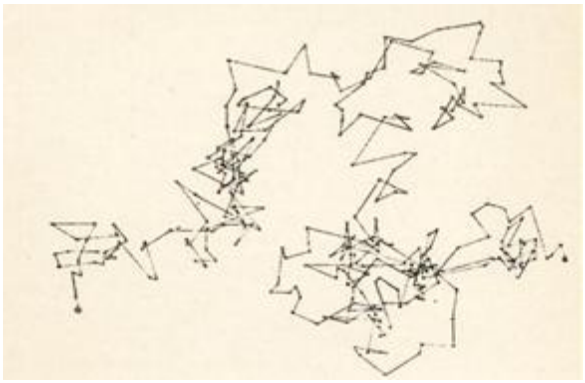

Figure 1.8*:Random paths of pollen grains molecules in water.*

This type of motion the particles start to spread all over the water with time. Diffusion occurs due to the unequally distributed concentration of pollen grains particles in the solvent which is water in this case. The tendency of the solute to have a uniform distribution all over the water cause the change in concentration due to the change in position flux J which is given by Fick's first law of diffusion as follows [5]:

$$J = -D\nabla\varphi \tag{1.1}$$

Where J is the diffusion flux: $[\,\mathrm{mol}\cdot\mathrm{m}^{-2}\cdot\mathrm{s}^{-1}\,]$, D represents the diffusion coefficient or diffusivity: $[\,\mathrm{m}^{2}\cdot\mathrm{s}^{-1}\,]$ and φ is the concentration: $[\,\mathrm{mol}\cdot\mathrm{m}^{-3}\,]$. Fick's second law Along with mass conservation is given below [6]:

$$\frac{\partial\boldsymbol{\varphi}}{\partial\boldsymbol{t}}+\frac{\partial\boldsymbol{J}}{\partial\boldsymbol{x}}=\mathbf{0}\Longrightarrow\frac{\partial\boldsymbol{\varphi}}{\partial\boldsymbol{t}}=\boldsymbol{\nabla}\cdot(\mathbf{D}\boldsymbol{\nabla}\boldsymbol{\varphi}) \tag{1.2}$$

Assuming the diffusion coefficient D to be a constant, we can exchange the orders of the differentiation and multiply by the constant:

$$\frac{\partial\varphi}{\partial\mathrm{t}}=\mathrm{D}\nabla^{2}\varphi \tag{1.3}$$

The solution of this equation is [5]:

$$\varphi(x,t) = \frac{\varphi_0}{\sqrt{4\pi Dt}} \exp(-\frac{x^2}{4Dt}) \tag{1.4}$$

a) Diffusion in Free Medium:

In isotropic medium, the diffusion is given by [5]:

$$p(r,t|r_0) = \frac{1}{\sqrt{(4\pi Dt)^3}} \exp(-\frac{\|(r-r_0)\|^2}{4Dt}) \tag{1.5}$$

and the distance change from $r_0$to r is shown in this relation:

$$<\|r\text{-}r_0\|^2> = 6Dt \tag{1.6}$$

However, it is not the same in anisotropic medium because D is not a constant coefficient, but a second-order tensor, which is represented by a 3×3 positive definite symmetric matrix [7].

$$D = \begin{bmatrix} D_{xx} & D_{xy} & D_{xz} \\ D_{xy} & D_{yy} & D_{yz} \\ D_{xz} & D_{yz} & D_{zz} \end{bmatrix} \tag{1.7}$$

Due to obstacles encountered by diffusing water molecules in biological samples, diffusion coefficient D is lower than that observed in "free" water meaning that when $< ||r - r0||2 >= 6Dt$ is used to compute the diffusion coefficient. This last is referred as the apparent diffusion coefficient (ADC).

b) Diffusion in complex medium:

In impermeable spheres the water molecules inside each sphere diffuse within the restricted space of that sphere, and the water molecules outside the spheres move randomly around them. Since there is no penetration through that sphere, the expected displacement distance is reduced. If the diffusion time interval is sufficiently long, the PDF will be more or less bell shaped and narrower than that of unrestricted diffusion (Figure 1.9(a)). Where for Hindered diffusion that occurs in semi-permeable spheres, water molecules cross with some resistance. The PDF is not as narrow as that of a volume containing impermeable spheres however it is narrower than that of a volume with free diffusion. But the PDF is still isotropic.

The case where the PDF is anisotropic can be found in the neuronal tissues that consist of tightly packed and coherently aligned axons and surrounded by glial cells forming bundles. The micrometric movements of water molecules are highly hindered in the direction perpendicular to the axonal orientation compared to the parallel to it which makes the molecular displacement parallel to the fiber typically greater than those who are perpendicular to it for both single [8] (Figure 1.9(b) and various orientations(Figure 1.9(c)).

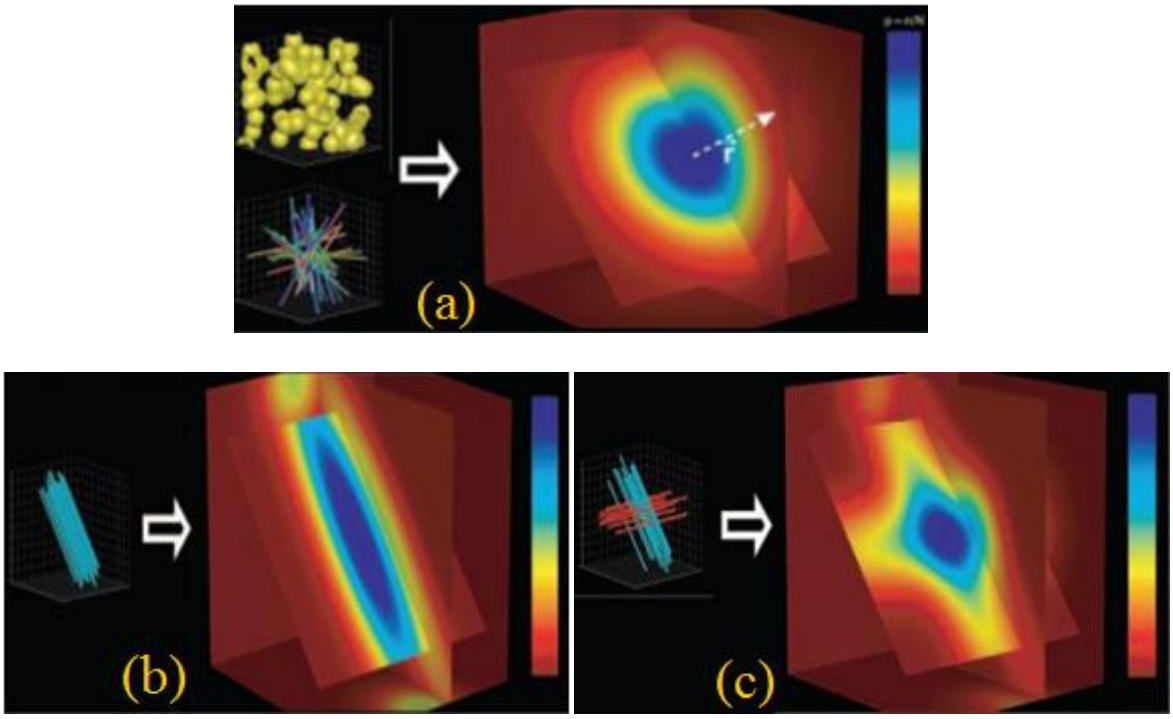

Figure 1.9*: (a) PDF in restricted diffusion (isotropic), (b) Single orientation (looks like cigar shaped) PDF and (c) Various orientations.*

1.2.2 How to measure diffusion with MRI?

a) Stejskal-Tanner's method:

Stejskal and Tanner introduced pulsed gradients into the basic spin echo sequence which made a great diffusion sensitivity improvement compared to the steady state gradients. They solved the Bloch-Torrey partial differential equations for a symmetric pair of pulsed gradients and obtained the well-known Stejskal-Tanner formula:

$$S = S_0 e^{-bD} \tag{1.8}$$

where:

$$b = \gamma^2 G^2 \delta^2 (\Delta - \frac{1}{3}\delta) \quad (1.9)$$

In Eqs (I.8) and (I.9), S is the signal strength in a pulse sequence with a pair of balanced diffusion-sensitizing gradients of strength *G*, each of a duration δ and with a delay Δ between them. S_0 is the signal strength in an identical experiment but without the diffusion gradient pair [9].

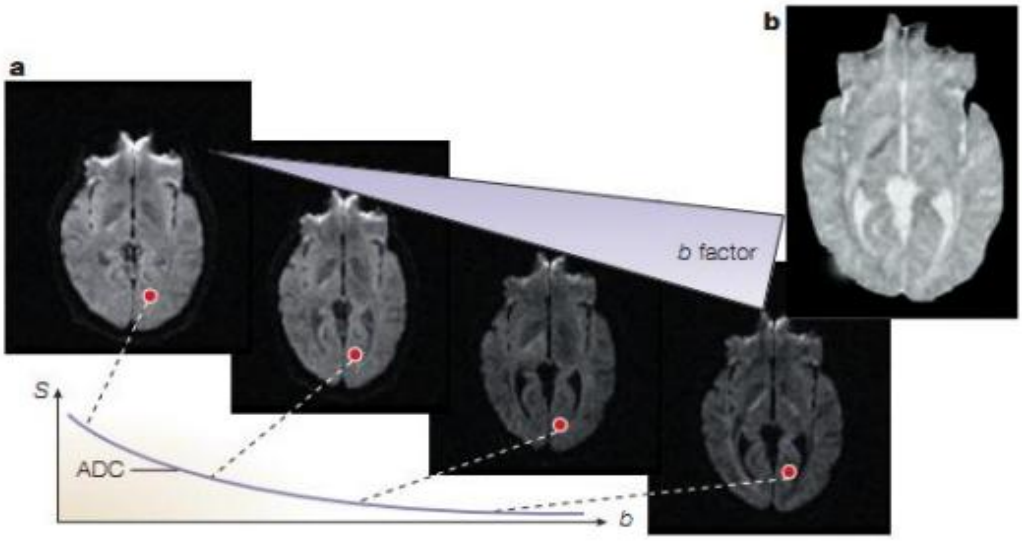

Figure 1.10*: The variation of S with respect to b (inversely proportional).*

b) Δ Effect:

Q-space is always sampled for a specific diffusion time interval. The longer the diffusion time interval is the better the directional resolution will be because within an axon a short diffusion time interval, there is a similar amount of diffusion in every direction so the axon direction cannot be distinguished. However for a longer interval, diffusion perpendicular to the direction of the axon tends to stop when the molecules reach the axon wall while diffusion along the long axis of the axon keeps propagating. A longer interval increases the distinction between the signals in the different directions but it also leads to a lower signal-to-noise ratio (SNR) [10].

c) Signal-to-Noise Ratio (SNR):

The Signal-to-Noise Ratio (SNR) is an important quantity used to evaluate the behavior and the performance of a given magnetic resonance imaging (MRI) system to compare many

aspects such as image quality, contrast enhancement value, pulse sequence and so on. And for a single image voxel r = (x,y,z) it is defined by (σ: the standard deviation and $S(r) \gg \sigma$:) :

$$SNR(r) = \frac{S(r)}{\sigma} \tag{1.10}$$

The most commonly used technique among the many available methods for determining SNR in MR Images is based on the signal statistics in two separate regions of interest (ROIs) from a single image: one in the tissue of interest to determine the signal intensity, the other one is the image background to measure the noise intensity. SNR measurements need to put two preconditions when using this "two-region" approach: the first one is that a spatially homogeneous distribution of noise over the whole image is required. The second one, for the noise properties measured in a background area to be used in deducing the noise distribution overlaying the anatomic structures in the foreground, the statistical intensity distribution of the noise should be known [11].

d)PDF and q-space:

Similar to k-space that is the Fourier reciprocal to the Image space. The PDF space and the q-space are just a Fourier pair $S = FT[P_\Delta]$,assuming that the PDF transitional invariant [10]:

$$P_\Delta(r'|r) = \bar{P}_\Delta(r' - r) = P_\Delta(\boldsymbol{R}) \tag{1.11}$$

Let $q = \gamma\delta g$, the acquired diffusion signal is:

$$S(\boldsymbol{r}, \boldsymbol{q}) = S_0(\boldsymbol{r}) \int P_\Delta(\boldsymbol{R})\, e^{i\boldsymbol{q}.\boldsymbol{R}} d\boldsymbol{R} \tag{1.12}$$

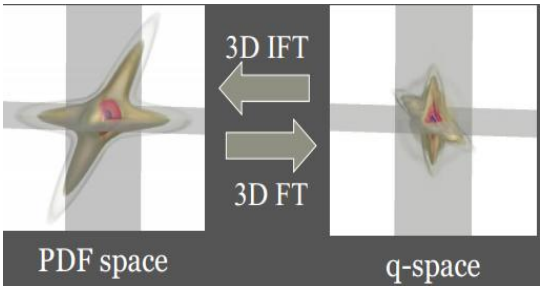

Figure 1.11*: PDF space and q-space are a Fourier pair.*

e) From PDF to ODF:

For each brain location, we reconstruct the Probability Density Function (PDF) by evaluating the discrete 3D inverse Fourier transform of the signal modulus sampled in q-space.

The result, called a *diffusion map*, is a 6-dimensional image that associates a three-dimensional diffusion function with every brain position voxel. From this map, at each voxel, we compute an Orientation Density Function (ODF) $\Phi(\mathbf{u})$, by projection of the PDF in the radial direction. If $\mathbf{u}$ is a 3D vector with $|\mathbf{u}|=1$ [1], we define:

$$\Phi(u) = \int p(\rho u)\rho^2 d\rho \tag{1.13}$$

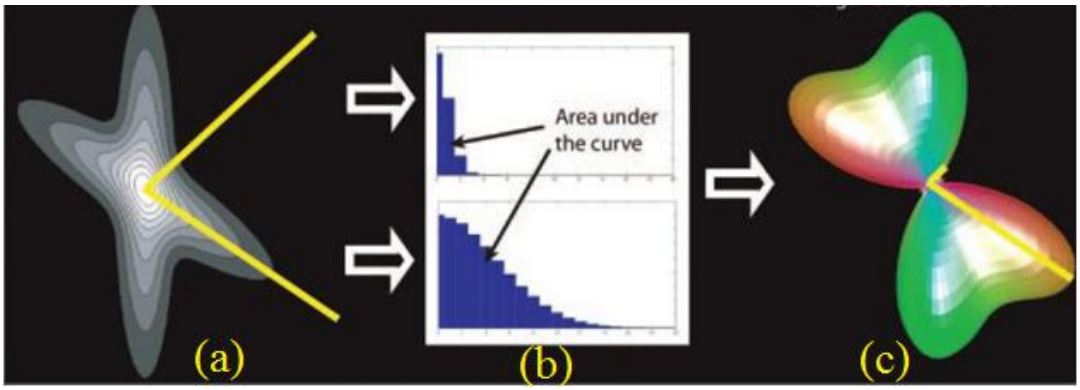

Figure 1.12*: Full diffusion PDF in 2D (a) Diffusion PDF along two arbitrary directions (b) the length of the radius of ODF is the sum of areas under the curve (c).*

1.3 Summary:

In this chapter, we have seen the physical and chemical theory laying behind dMRI as well as the mathematical background that helped improving it more and more with the effort of the researchers and scientists interested in medical imaging field.

From dMRI Reconstruction Models to Brain Tractography

In this chapter we will cover the well-known dMRI reconstruction models and explore the inter-phases steps that must be accomplished before applying tractography methods to reveal the underlying brain structure.

2.1 Diffusion MRI techniques:

2.1.1 Diffusion-weighted imaging (DWI):

Le Bihan used in diffusion encoding specific magnetic gradient pulses which required mixing of such pulses with those used in the MRI sequence for spatial encoding using the work of Stejskal and Tanner in the 1960s, He introduced the 'b factor' in his first paper about diffusion MRI (derived from his name, "B"ihan). Diffusion-weighted MR imaging is the simplest form of diffusion imaging. The image intensity partly reflects information of microstructures in terms of diffusion (splenium and ventricles) [12].

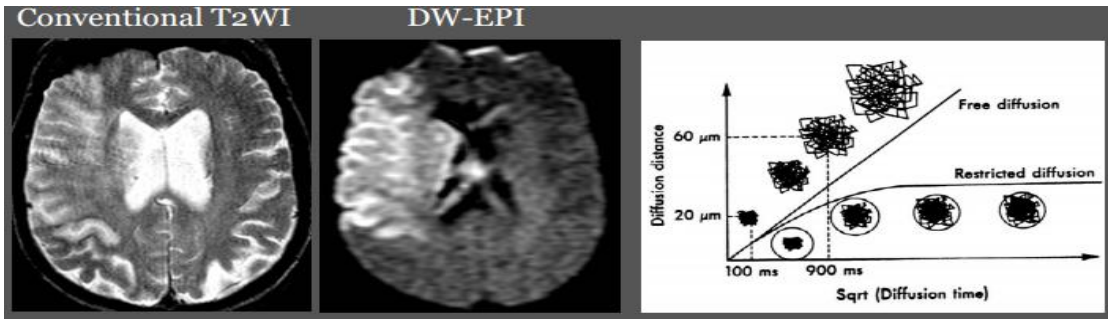

Figure 2.1*: Diffusion distance versus square root of diffusion time.*

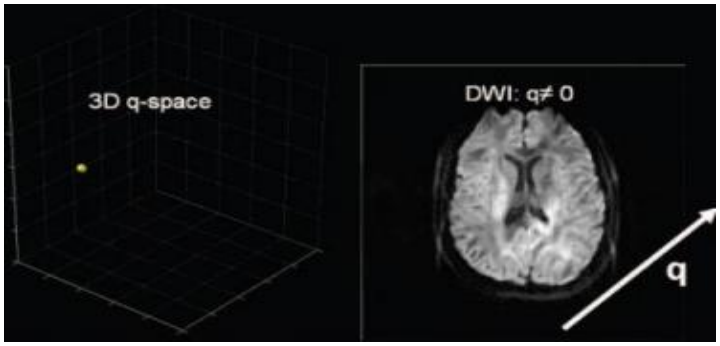

Figure 2.2*: Diffusion-weighted MR imaging corresponds to one point in q-space.*

The problem of diffusion-weighted imaging is that the interpretation of the resultant images is not intuitive. Under the free-diffusion model, which is a 3D isotropic Gaussian distribution, the apparent diffusion coefficients (ADC) [12] would be introduced here and could be derived by:

$$ADC = -\frac{1}{b} log \frac{S}{S_0} \quad (2.1)$$

To obtain ADC values, we need two acquisitions to be satisfied. The first one is that researchers realized the great dependency of image intensities on the directions of the diffusion gradients, Hence on ADC. The second one is that one can perform three orthogonal measurements and average the result to obtain a better approximation of the diffusion coefficient.

$$ADC = \frac{1}{3}(ADC_x + ADC_y + ADC_z) \tag{2.2}$$

2.1.2 Diffusion Tensor Imaging (DTI):

A diffusion tensor is a 3x3 symmetric, positive-definite matrix which has 6 unique elements (symmetric) and suffices to estimate the upper (lower) triangular part and positive-definite because all eigenvalues are positive [12]. It is given by the following matrix:

$$D = \begin{bmatrix} D_{xx} & D_{xy} & D_{xz} \\ D_{yx} & D_{yy} & D_{yz} \\ D_{zx} & D_{zy} & D_{zz} \end{bmatrix} = [e_1, e_2, e_2] \begin{bmatrix} \lambda_1 & 0 & 0 \\ 0 & \lambda_2 & 0 \\ 0 & 0 & \lambda_3 \end{bmatrix} [e_1, e_2, e_3]^{-1} \tag{2.3}$$

Tensors can be displayed as ellipsoids: If λ1 is the maximum eigenvalue, then e1 is called the principal direction on the tensor. In DTI, e1 is usually assumed to coincide with the fiber orientation [13].

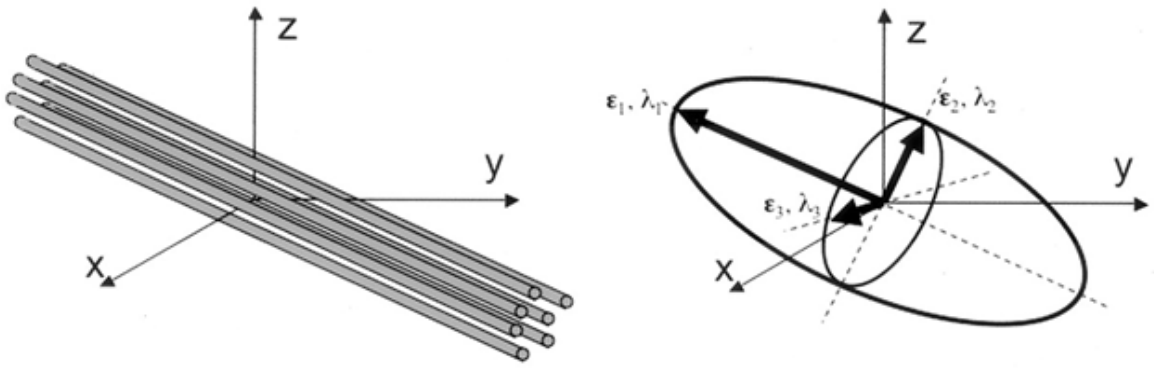

Figure 2.3*: Tensor representation as ellipsoid.*

Diffusion tensors are into two main categories:

1. Isotropic diffusion tensor which contains the spherical shaped tensor (where $\lambda_1 = \lambda_2 = \lambda_3$).

2. Anisotropic diffusion tensor fall into two cases which are (i) linear shaped (cigarette shaped) ($\lambda_1 > \lambda_2 > \lambda_3$) and (ii) planar shaped ($\lambda_1 = \lambda_2 > \lambda_3$).

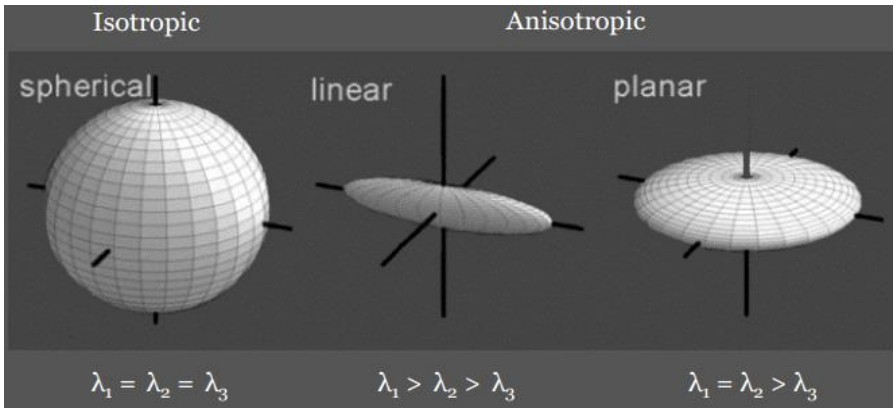

Figure 2.4*: Different forms of diffusion tensor representation based on the isotropy.*

In 1994, Basser et al. introduced the DTI method. Assuming water diffusion remains Gaussian but may be anisotropic. They used a second-order tensor to describe such model. They used the Stejskal-Tanner sequence which can be defined by six parameters to measure the tensor, these parameters describe the variance of the diffusion along the three primary axes, we can derive several measures using these parameters but we are interested mainly on the principal eigenvector of the tensor having the highest eigenvalue λ1, the direction of the local diffusivity is along the direction of this eigenvector.

At least six points in q-space with q≠0 (DWI) and one point with q=0 (reference image) are required to be sampled (Fig 2.5), with a condition that the directions of the six q points must be non-colinear in order to fit the model. So six DWI images + one T2W image are required for a complete DTI measurement. Each voxel must have its own diffusion tensor and a peak-from-model obtained from it (Fig 2.6 and 2.7) [8].

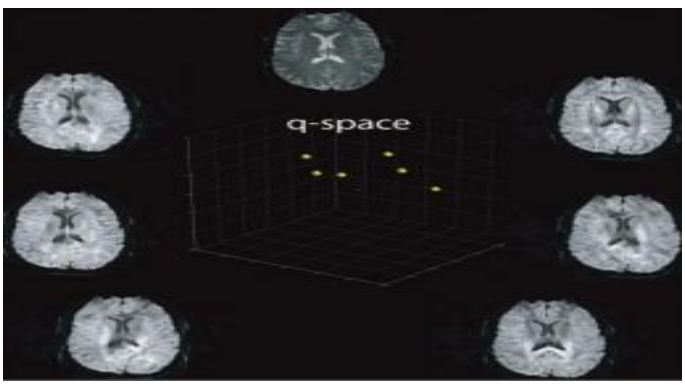

Figure 2.5*: Six points in q-space with q≠0 (DWI) + one point with q=0 are required in DTI.*

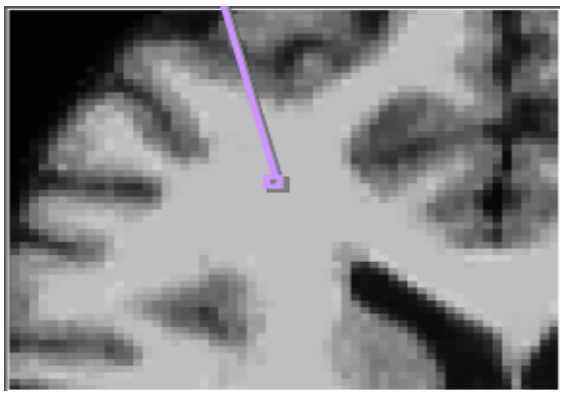

Figure 2.6*: An intensity image at each voxel.*

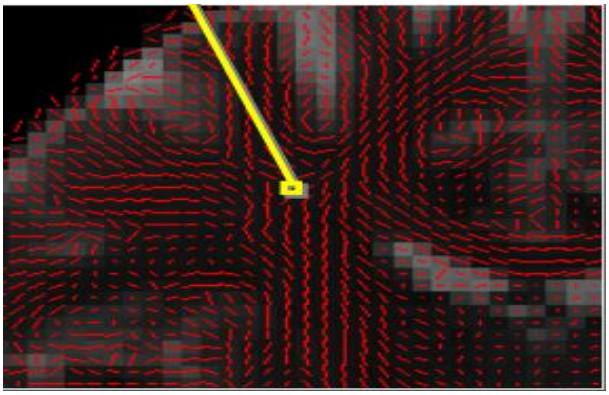

Figure 2.7*: A tensor peak map at each voxel.*

Basser et al. showed that [13]:

$$S(r) = S_0(r)\exp(-bg^T D(r)g) \tag{2.4}$$

The elements of the tensor could be obtained by:

$$\begin{aligned} D_{xx} &= -\frac{1}{b}\log\left(\frac{S_{xx}}{S_0}\right) \\ D_{yy} &= -\frac{1}{b}\log\left(\frac{S_{yy}}{S_0}\right) \\ D_{zz} &= -\frac{1}{b}\log\left(\frac{S_{zz}}{S_0}\right) \\ D_{xy} &= -\frac{1}{b}\log\left(\frac{S_{xy}}{S_0}\right) \\ D_{xy} &= -\frac{1}{b}\log\left(\frac{S_{xz}}{S_0}\right) \\ D_{yz} &= -\frac{1}{b}\log\left(\frac{S_{yz}}{S_0}\right) \end{aligned} \tag{2.5}$$

$$D = \begin{bmatrix} D_{xx} & D_{xy} & D_{xz} \\ D_{xy} & D_{yy} & D_{yz} \\ D_{xz} & D_{yz} & D_{zz} \end{bmatrix} \tag{2.6}$$

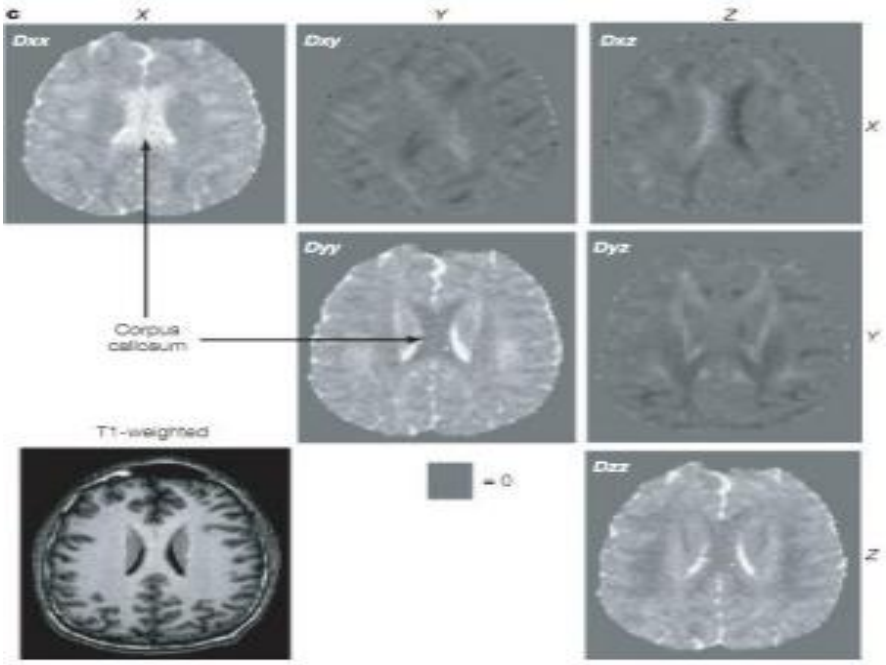

Figure 2.8*: Tensor visualization at each matrix component.*

For multiple acquisitions (N>6), the tensors could be estimated via linear fitting.

$$S_i = S_0\, exp(-b g_i^T D g_i) \Longrightarrow -log\left(\frac{S_1}{S_0}\right) = \sum_{j=1}^{6} b_{ij} D_j \tag{2.7}$$

$$\begin{aligned} -\log\left(\frac{S_1}{S_0}\right) &= b_{11}D_1 + b_{12}D_2 + b_{13}D_3 + b_{14}D_4 + b_{15}D_5 + b_{16}D_6 \\ -\log\left(\frac{S_2}{S_0}\right) &= b_{21}D_1 + b_{22}D_2 + b_{23}D_3 + b_{24}D_4 + b_{25}D_5 + b_{26}D_6 \\ -\log\left(\frac{S_N}{S_0}\right) &= b_{N1}D_1 + b_{N2}D_2 + b_{N3}D_3 + b_{N4}D_4 + b_{N5}D_5 + b_{N6}D_6 \end{aligned} \tag{2.8}$$

$$X = Bd \;\Longrightarrow d = (B^T B)^{-1} B^T X \tag{2.9}$$

a) Statistical measurements:

From the diffusion tensor matrix, many statistical measures [12] that characterize the diffusion can be calculated:

- Axial diffusivity (AD):

The scalar of the greatest eigenvalue of the three eigenvalues and it represents the diffusion along the first eigenvector:

$$\boldsymbol{AD = \lambda_1} \tag{2.10}$$

- Mean diffusivity (MD):

It is the measurement of the average diffusion in general at that tensor; it is typically much higher in CSF (Cerebrospinal fluid) than in the WM (white matter):

$$\boldsymbol{MD = \bar{\lambda} = \frac{\lambda_1 + \lambda_2 + \lambda_3}{3}} \tag{2.11}$$

- Radial diffusivity (RD):

It is a measure of the average perpendicular diffusion (mean of the two lower eigenvalues) to the first eigenvector (main diffusion direction):

$$\boldsymbol{RD = \frac{\lambda_2 + \lambda_3}{2}} \tag{2.12}$$

- Fractional anisotropy (FA):

It is the degree of anisotropy which represents the deviation from isotropic diffusion. It is appropriately normalized so that it takes values from zero (when diffusion is isotropic) to one (when diffusion is constrained along one axis only). It is calculated as the variance of the three eigenvalues.

$$\boldsymbol{FA = \sqrt{\frac{3}{2}\frac{(\lambda_1 - \bar{\lambda})^2 + (\lambda_2 - \bar{\lambda})^2 + (\lambda_3 - \bar{\lambda})^2}{\lambda^2 + \lambda^2 + \lambda^2}}} \tag{2.13}$$

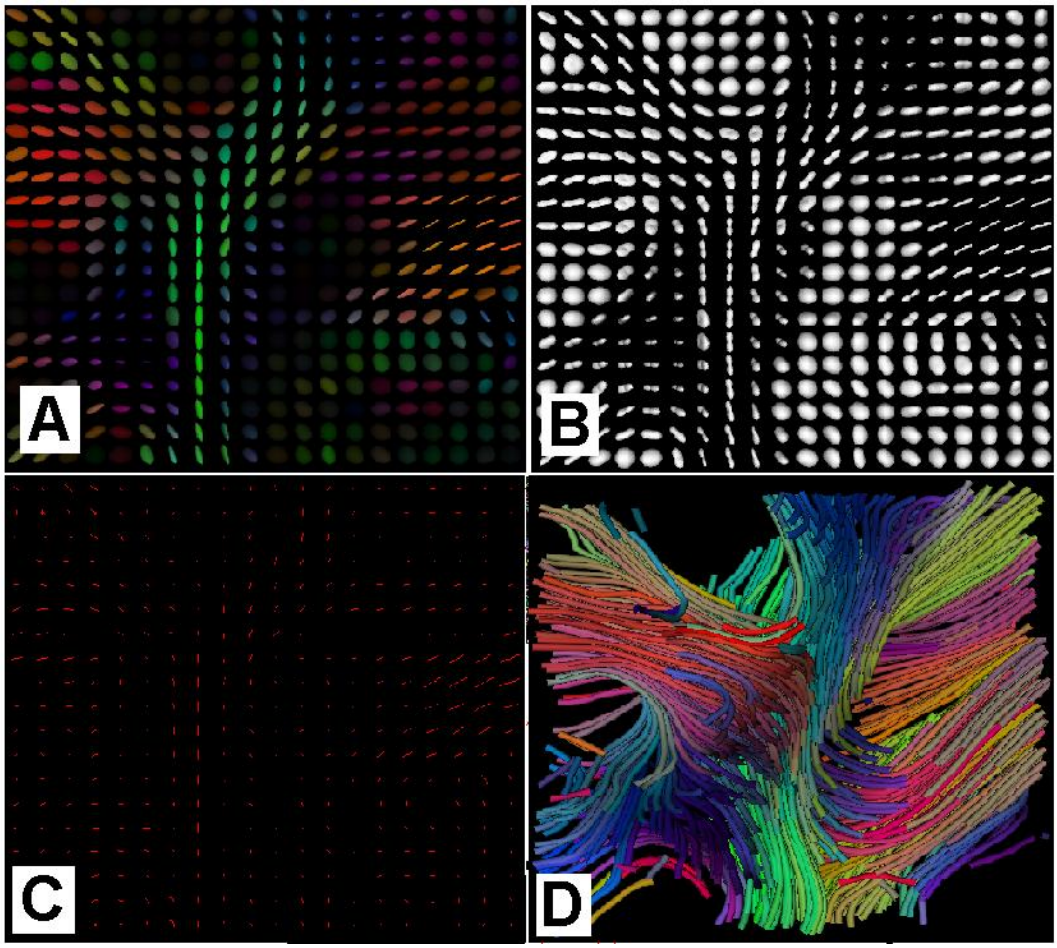

Figure 2.9 *The tensor models(DTI) (A) and its corresponding ODF representation (B) and Peaks-from-model segments (it will be covered in this chapter) (C) to be used in showing tracts (fibers) using tractography(it will be covered in this chapter)(D) for a region in the CC (Corpus Callosum).*

b) Limitations of DTI:

Single compartment has one fiber in each voxel while more than 30% voxels in the brain contain at least two fibers. Furthermore, Gaussian distribution May not be true since it is usually restricted diffusion [12] (fig2.10).Also, It is known that using DTI to obtain results in regions where WM fibers cross is incapable of describing those multiple fiber orientations within an individual (see Fig 2.11). Therefore, DTI is only valid for unidirectional fiber bundles that are large compared to the voxel size.

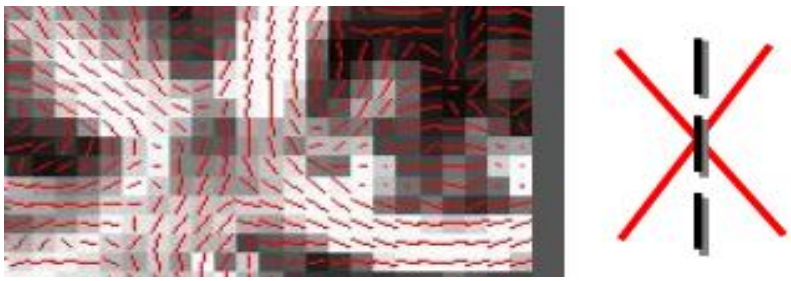

Figure2.10: *The number of fibers may be greater than one in each voxel.*

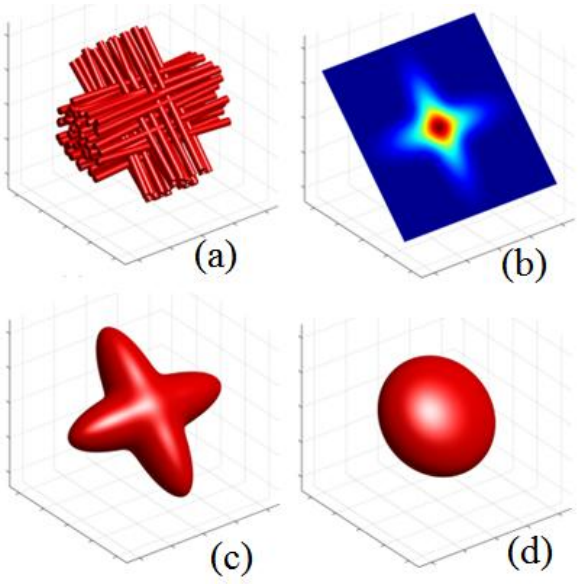

Figure 2.11*: Diffusion in an environment with multiple fiber populations the true diffusion PDF (b) and its isoprobability surface (c) are able to characterize the underlying fiber populations (a), the diffusion tensor model can not characterize the real fiber crossing (d).*

For these previous limitations, there is an increasing interest in introducing more adequate models than the DT that are able to resolve multiple fiber orientations in a single voxel using more complex approaches.

2.1.4 Diffusion Spectrum Imaging (DSI):

In 2000, Wedeen et al. [14] developed Diffusion Spectrum Imaging DSI, the most comprehensive diffusion MRI method. Its dataset is 6D, 3D of image space are obtained when the spatial position are sampled in *k*-space while the other 3D are acquired when q-space samples the space of the spin displacements [12]. It measures the diffusion PDF p(r) directly by applying the inverse Fourier transform on the q-space samples $A(q) = S(q)/S(0)$ as follows:

$$p(\boldsymbol{r}) = F^{-1}\left[A(\boldsymbol{q})\right](\boldsymbol{r})$$

The discrete representation of $p(r)$ we get from the IFFT is not directly useful for estimating the fiber orientations, since it is a function of 3D space. In practice, one usually calculates the diffusion orientation density function (dODF) $\psi(\hat{r})$ which is the projection of p onto the unit-sphere [15]:

$$\psi(\hat{r}) = \int_0^\infty p(\propto \hat{r})\, d \propto$$

where $\hat{r} = r/\|r\|$ is a unit-vector in the direction of r. $\psi(\hat{r})$ is evaluated for each finite set of directions $\hat{r}$ by taking steps along the line in direction$\hat{r}$ then interpolating the discrete p to estimate its value at each step and accumulating the values over all steps. The main limitation of DSI is the large amount of data required to perform the inverse Fourier transform and the correspondingly long acquisition time.

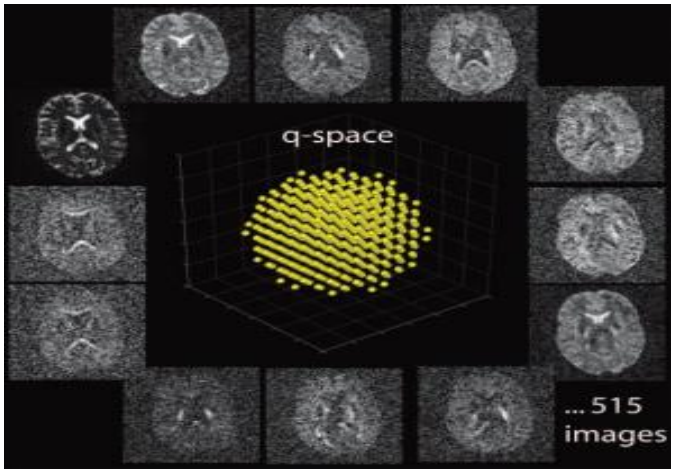

Figure 2.12*: DSI requires about 515 DW Images.*

- ***Generalized fractional anisotropy (GFA):***

Through ODF, we can define a scalar parameter analogous to FA of DTI, called GFA [12].

$$GFA = \frac{std(\psi)}{rms(\psi)} = \sqrt{\frac{n}{n-1}\frac{\sum_{i=1}^{n}(\psi(u_i) - \bar{\psi})^2}{\sum_{i=1}^{n}\psi(u_i)^2}} \tag{2.14}$$

$$\bar{\varphi} = \frac{1}{n}\sum_{i=1}^{n}\psi(u_i) \tag{2.15}$$

where:$0 \leq GFA \leq 1$

2.1.3 Q-ball imaging (QBI):

DSI practically has a long acquisition requirement; many techniques have been proposed to overcome this problem. In 2004, Tuch [15] introduced one of the methods of high angular resolution diffusion imaging (HARDI). Q-ball imaging, dODF are directly estimates by QBI using a shorter and more efficient high-angular resolution diffusion

imaging (HARDI) acquisition [15] which samples the q-space only at a fixed q-space radius, resulting in a high angular density spherical acquisition scheme (Figure 2.14). QBI approximates the dODF $\psi(\hat{r})$ by the Funk-Radon transform (FRT) of the HARDI signal S(q) .

$$\psi(\hat{\boldsymbol{r}}) \approx \int_{\substack{q \perp \hat{\boldsymbol{r}} \\ \|\boldsymbol{q}\| = \boldsymbol{q}'}} S(\boldsymbol{q})\, d\boldsymbol{q} \tag{2.16}$$

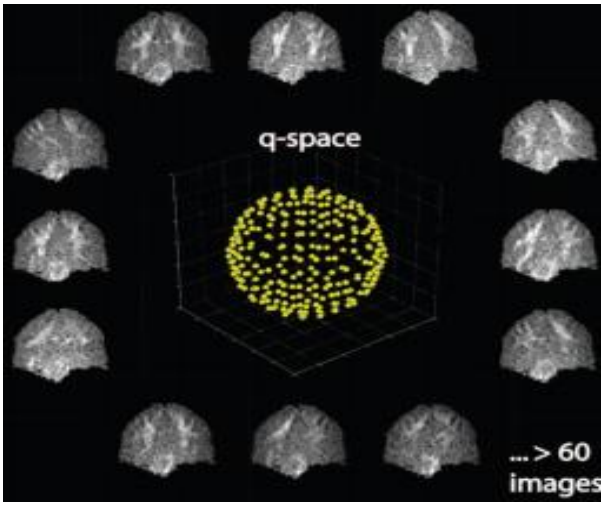

Figure 2.13 : *q-space requires more than 60 DWI*

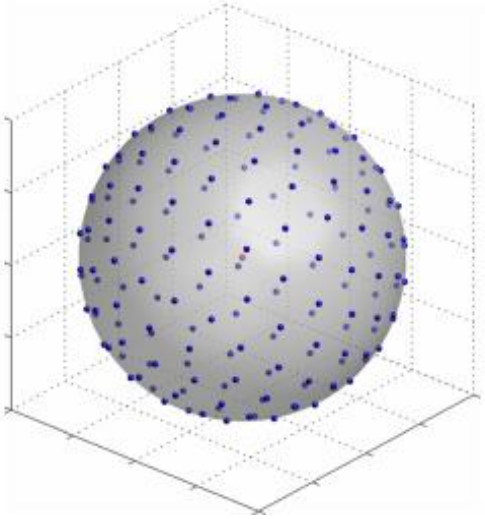

Figure 2.14 *: HARDI q-space sampling*

When dMRI acquisition use only a single b-value this is often called single shell HARDI [16,17]. Spherical harmonics (SH) is a mathematical function which provides the sphere's orthonormal basis the usage of this mathematical function is the approximation of spherical function like orientation Distribution function (ODF) from low frequency to a highest frequency which called SH order as follows [12].

$$\hat{S}(q) = \sum_{l=0}^{l_{max}} \sum_{m=-l}^{l} c_l^m \, \acute{Y}_l^m(q) \tag{2.17}$$

Substitution of Eq.(2.17) into Eq.(2.16) and after rearranging the resulting equation, we get:

$$\psi(\hat{\boldsymbol{r}}) \approx \sum_{l=0}^{l_{max}} \sum_{m=-l}^{l} c_l^m \int_{\substack{q \perp \hat{\boldsymbol{r}} \\ \|\boldsymbol{q}\| = \boldsymbol{q}'}} \acute{Y}_l^m(\boldsymbol{q})\, d\boldsymbol{q} \tag{2.18}$$

FRT can be done analytically on the modified spherical harmonics basis functions:

$$\int_{\substack{q\perp\hat{r}\\ \|q\|=q'}} \acute{Y}_l^m(\boldsymbol{q})\, d\boldsymbol{q} = 2\pi P_l(0)\acute{Y}_l^m(\hat{\boldsymbol{r}}) \tag{2.19}$$

where $P_l(.)$ are the unassociated Legendre polynomial of order l. so the ODF can be computed from SH representation that follows:

$$\psi(\hat{\boldsymbol{r}}) \approx \sum_{l=0}^{l_{max}} \sum_{m=-l}^{l} 2\pi P_l(0)\ \acute{c}_l^m Y_l^m(\hat{\boldsymbol{r}}) \tag{2.20}$$

In other words, if $\boldsymbol{f}$ and $\boldsymbol{s}$ are the $n_c \times 1$ SH coefficient vectors of $\psi(\hat{\boldsymbol{r}})$ and $\hat{S}(q)$, respectively, and Q is the $n_c \times n_c$ diagonal matrix with $Q_{jj} = 2\pi P_{l_j}(0)$ where l_j= (0, 2, 2, 2, 2, 2, 4, 4, 4, 4, 4, 4, 4, 4, 4, ...), the FRT can be performed directly on the SH coefficients as a single matrix multiplication:

$$\boldsymbol{f} = \boldsymbol{Q}\boldsymbol{s} \tag{2.21}$$

2.1.4 Constrained Spherical Deconvolution (CSD):

To improve the angular resolution of the reconstruction (AR) in QBI which reconstruct the diffusion ODF (dODF), Tournier et al (2004) [18] introduced spherical deconvolution (SD to reconstruct the fiber ODF. As the name stands, SD can be performed using a matrix inversion but it has a noise effect [18], so Constrained Super-resolved spherical deconvolution (CSD) [19] gives a solution to this problem by applying two major constraints on the fitting of the fODF. The first is that it applies a non-negativity constraint: fODF values that are smaller than zero are non-physical and are precluded. The other is that CSD assumes that only a few of the fODF values will be large. Applying these two constraints allows fitting the SH basis up to very high orders, in essence fitting more parameters than the data allows.

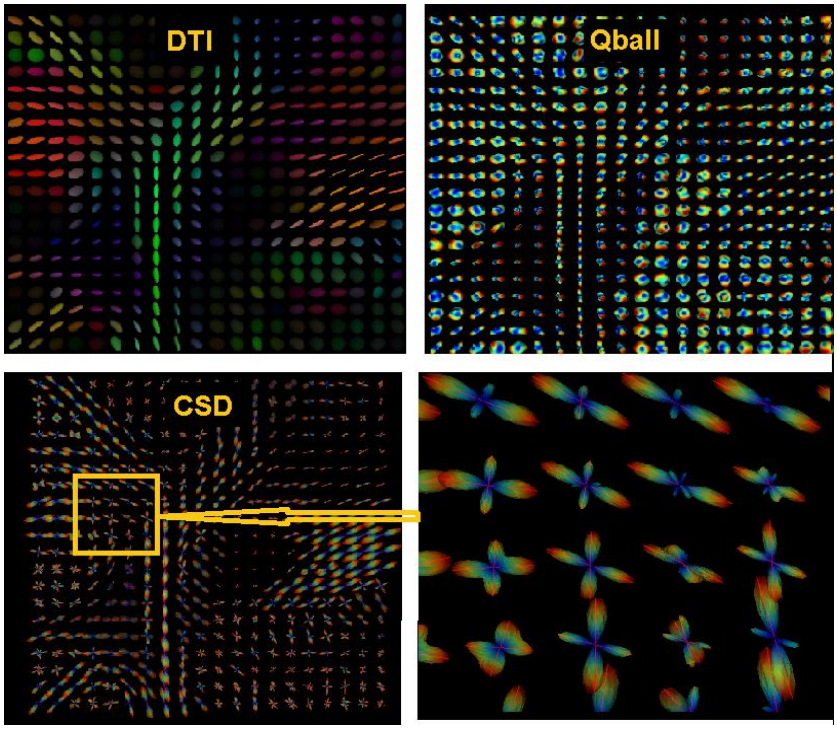

Figure 2.15 *comparing between different methods of reconstruction (CSD,DTI and Q-ball).*

2.1.5 Peaks from Models:

ODF function is used to visualize the local orientations on every voxel; they can be obtained from any reconstruction models such as DTI, Q-ball and DSI enabling us to find the directions of the maxima in the ODFs (which can be useful for tracking). Tractography methods are used to show the brain pathways or fibers by joining the local Peaks-from-Model segments to generate the whole pathway of the brain (or a part of it) [12].

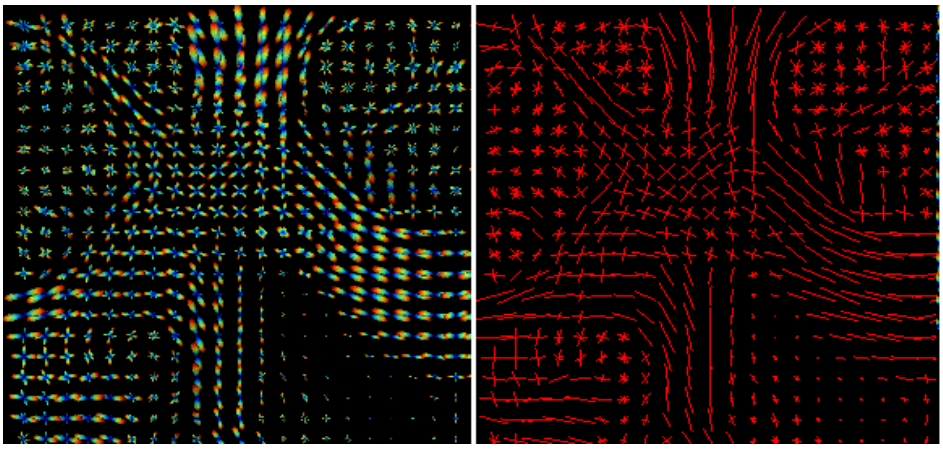

Figure 2.16 : *CSD models as shown using our software.*

Figure 2.17 : *The peaks obtained using our software.*

2.2 Tractography Methods:

In neuroscience, tractography is a 3D modeling technique that uses as input the data collected from one of the reconstruction methods by piecing together the local WM (white matter) to build long connectivity patterns between brain regions. It is the only tool to visualize non-invasively and in-vivo neuronal fibre tracts in the human brain.

Tractography methods are classified in three categories: a) local, b) global and c) simulated. Local approaches propagate a curve from a starting (seed) point using locally greedy criteria, i.e. tracking sequentially through orientation estimates in adjacent voxels. Global approaches identify the best path between two points of interest, according to some optimization criterion, rather than identifying paths arising from a single point. Simulated approaches constitutes of algorithms that simulate the diffusion process or solve the diffusion equation to reconstruct white matter tracks. A detailed explanation about them is following.

2.2.1 Local Approach:

a) Deterministic method:

Deterministic tractography was the first to appear. It assumes a single orientation at each voxel. Streamlines (or tracks) are created as paths in the form of polylines along an initial direction at a specific point called the "seed" in the 3D volume. In FACT [2] (Fiber Assignment by Continuous Tracking) method tracks are spread in unequal steps controlled by the starting point of the streamline in the voxel (see Figure below).

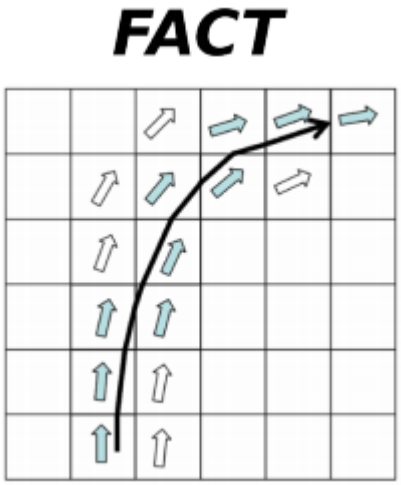

Figure 2.18*: The FACT method for fiber tracking.*

Euler integration with equal steps was used in Conturo et al. [20] and also Runge-Kutta integration was used in Basser et al. [21] Deterministic approaches usually stop propagating when it come to a low anisotropy region (usually FA < 0.2) is found. This is useful in order to avoid propagation within the CSF region (in fact, tracts do not exist anatomically in this region) or within deep gray matter regions where tracking is not certain. Also, they usually check for large angular changes (e.g. larger than 90) between successive steps (this represent sharp turns which are unrealistically and should be avoided).

Deterministic methods can also be used in the case when multiple orientations are estimated in a single voxel (crossing fibres). These orientations can be obtained for example as the principal eigenvectors of multiple Tensors fitted to the data [22], or from the local peaks of the diffusion ODF estimated using DSI[23] and QBI [15] or from the orientations from the fibre ODFs [24]. There are various approaches for propagating across voxels where more than one fibre orientation has been identified. One approach is, upon entering a voxel, to choose the orientation that produces the smallest curvature with the incoming path used in Wedeen et al. [25]. Another approach follows all orientations that do not overpass a curvature threshold, by initiating a new streamline per orientation using in Chao et al. [26] and Descoteaux et al. [27]. An interesting point that should be marked is that most methods of this category utilize only the fibre orientation estimates. Tensor deflection tractography (TEND) proposed by Lazar et al. [28] is a FACT variant that utilizes the whole DTI Tensor instead of just its principal eigenvector to get the direction of curve propagation.

b) Probabilistic method:

Probabilistic tractography was firstly introduced by Parker et al. [29], and Behrens et al. [30], here the standard procedure is performed by computing a spatial distribution of probable tracks starting from a single seed rather than a single track. In each propagation step of each streamline, a random perturbation of the underlying fibre orientation estimate is followed. Perturbations are created using functions that characterize the uncertainty in the fiber orientation within each voxel. A probabilistic index of connectivity (PICo) is defined between a seed and an arbitrary point as M/N; where N is the number of all the tracks that start from the seed and M is the number of tracks that traverse the seed and the arbitrary point.

Probabilistic approaches mainly vary in the way that the orientation uncertainty is evaluated and estimated. Most commonly, a Bayesian framework is used to compute the posterior probability of the reconstruction model's orientation parameters [30],[31], [32],

[33] and [34]. In Behrens et al Monte Carlo-Markov chain (MCMC) was used to sample the orientation posterior distribution while In Friman et al. [33] it was evaluated numerically after using Dirac priors. However, in Zhange et al. [34] particle filtering was used for the same purpose.

c) Bootstrap method:

Bootstrap tractography is second method that indicates the uncertainty of the fibre orientation. Pajevic et al. [35] and Lazar et al. [36] are two of the first to apply this method in dMRI. This is a non-parametric approach where a diffusion acquisition is repeated many times and generating by the way a large set of images for the same subject. Some images from this set are drawn in random with replacement. This process gives a single bootstrap sample. Drawing many samples will lead to a distribution for the fibre orientation. The advantage of bootstrap tractography is that no initial arranged assumptions are made on the noise and it is sensitive to all sources of variability that affect the acquired data set. The disadvantage is that many repeated acquisitions should be performed; According to O'Gorman et al [37], at least 5 for DTI are required.

2.2.2 Global Approach:

One of the limitations of probabilistic tractography is that the probabilistic index of connectivity decreases as the distance from the seed point increases. Another limitation is that it is un-negligibly sensitive to local noise. Global approaches try to find out solutions to these limitations by being distance-independent and by increasing resistance toward noise in a global term. These are accomplished by finding an optimal path between two voxels, according to a global property [38]. Jbabdi et al. [39] introduced a Global Bayesian model so as to get the posterior probability of connections. The path trajectories represented by splines are compatible with the local fibre orientations in regions with low uncertainty estimates. In regions with high uncertainty, the global connectivity information constrains the local parameter estimation and affects in turn the path sampling.

a) Front evolution method:

Front evolution *techniques* often employ fast marching techniques. The front spreads from the seed neighbours to the next neighbouring nodes with speeds given by the local fibre orientations. As the front propagates, a time of front arrival can be associated with each visited voxel. When all image voxels are crossed by the front, paths of connection can be obtained going backwards in the map of front arrival times. Starting from an arbitrary voxel,

a gradient descent algorithm can find the fastest way back to the starting point (seed). A connectivity index can be associated with each path, representing either the weakest link along the path or the agreement between the path tangents and the underlying vector orientation field (see Parker et al. [40], Tournier et al. [41], Cambell et al. [42], Fletcher et al. [43] and Gigandet et al. [44]).

b) *Graph-based* method:

Graph-based tractography *uses* weighted networks (graphs). This type of tractography is credited to Iturria-Medina et al. [45], Zalesky et al. [46], Lifshits et al. [47], Fillard et al. [48] and Sotiropoulos et al. [49]. The common principle of these approaches is that each image voxel becomes a node in the graph where the edges of the graph join pairs of neighbouring voxels or ROIs. The edges are assigned weights which allow them to be represented in any structural form. Anatomical paths are then defined as chains with successive elements being neighbouring voxels.

c) Energy Minimization method:

Energy Minimization method [50] tends to optimize all tracks from the whole brain volume at the same time. Each tract is represented as a chain of cylinders that are positioned and oriented in a changeable manner. The method aims to the set of cylinders that best approximate the underlying white matter bundles. This is achieved by minimizing the overall energy of all cylinders simultaneously, replicating natural phenomena. Kreher et al. [51], Reisert et al. [52], Lazar et al. [53] and Fillard et al. [54] showed results using energy minimization. Despite the very promising results shown by Reisert et al [52], the very high computation time was an important drawback of this framework.

d) Microstructure method:

Microstructure t*racking is* a really interesting new type of algorithms that combine global tractography and direct microstructure estimation under the use of diffusion weighted imaging data. Connectivity via tractography, axon diameter distribution and density estimates are all gathered and collected in order to inform one another given the common assumption that micro-structural features remain consistent along fibers. MicroTrack [55] is a recent example of this category. Algorithms of this type require their own acquisition schemes, similar to those employed in ActiveAx, developed by Alexander et al. [56].

2.2.3 Simulated approach:

This category of methods takes a very different approach compared to what we have seen till now. They simulate the diffusion of water molecules contained within the brain tissue or they can directly evaluate and solve Fick's second law of diffusion in the entire brain. In this category belong the work of Batchelor et al. [57], Kang et Al. [58], Hageman et al. [59] and Hagmann et al [60].

In Batchelor et al. [57], the diffusion equation is solved using a finite elements approach. Successive diffusion simulations of the whole brain, taking a seed as an initial position, are performed in Kang et al. [58]. Tractography by simulating fluid flow through a "pressure" Tensor field is performed in Hageman et al. [59]. The Navier-Stokes equation is solved using a finite elements approach. However, solve a partial differential equation increases in the other hand the execution time (which would make it unpractical). Furthermore, it is not always easy with these approaches to obtain a connectivity map across the whole brain volume and there are usually a huge number of parameters to set.

2.3 Summary:

In this chapter, we have covered the most known reconstruction models used in diffusion magnetic resonance imaging giving a general idea about their mathematical background (although it was not that deep because it was not the main point of this work), we have seen their advantages and drawbacks. We also knew how to get the peak-from-model using the ODF from these reconstruction models to be used later in tractography. This last could be implemented by so many different methods as we have seen that have distinct approaches and various work procedures with the same purpose which is giving the best evaluation and visualization of the brain underlying structure.

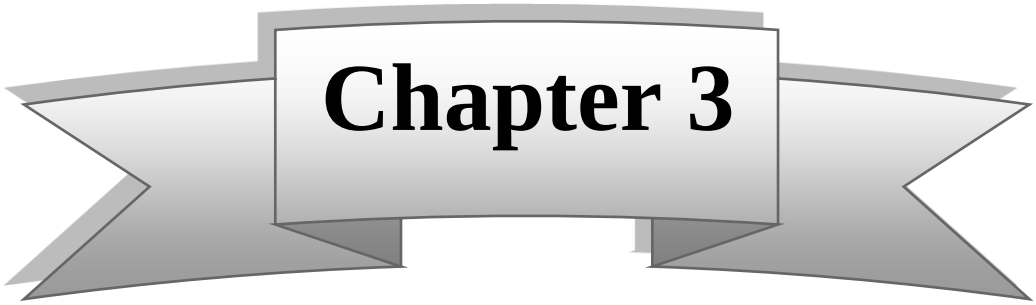

CIERTE A Proposed Deterministic Tractography Algorithm

In this chapter we are going to introduce our new tractography algorithm ,we call it CIERTE which stand for Combination of Improved Euler and Range-Kutta fourth-order algorithm with tracking Error, we are also going to study some tracking parameter like step size and seed points and see the effect of each one, finally we visualize the real brain tractography results.

3.1 INTRODUCTION:

As we have seen in the previous chapter, local tractography algorithms are classified into two largely categories deterministic and probabilistic most of this algorithms are linked to their reconstruction techniques.

In this work, we are going to use a purely deterministic algorithm, which is fast and accurate. Most importantly, it can have as input model-based or model-free reconstruction algorithms of most known algorithms; we call our algorithm "CIERTE" (Combined Improved Euler Range-Kutta using Tracking Error).

CIERTE has a lot of similarity with the EuDX algorithm, which can deal with any number of crossing fibers as long as the reconstruction algorithm supports them, the only difference between the EuDX and CIERTE is the method of integration through the streamlines, which is using Improved Euler with a combinational approach with the fourth-order Range-Kutta algorithm; this approach is applied by calculating a tracking error that would be used to apply the improved Euler or the Euler approximations.

3.2THE CIERTE ALGORITHM:

We designed an algorithm, which has similarities with most deterministic methods including classical and recent ones [61, 27, 62]. Our main purpose is to create a fast, accurate and general tractography algorithm, which can be used in different categories of anisotropy function as well as it, should work well in areas where multiple crossing fibers are present to make this algorithm general. We use the native space image coordinate by assuming the voxel dimensions are equal in all three dimensions, although we can go through a rescaling preprocessing step if the data is not the same size in the three dimensions.

In this new algorithm, we use streamline tractography [63], any line whose tangent is parallel to a local vector during its entire course known as a streamline through a vector field. Mathematically speaking a line can be represented as 3D space curve p(s), with $\boldsymbol{s}$ as the arc length for the streamline to align with the vector field the tangent at arc length $\boldsymbol{s}$ has to be equal to the vector at a corresponding position:

$$\frac{d\boldsymbol{p}(s)}{ds} = \boldsymbol{v}[\boldsymbol{p}(s)] \tag{3.1}$$

Where $\boldsymbol{p}(s)$ denotes the 3D position along the streamline and $\boldsymbol{v}$ is the 3D vectorfield.In the case of fiber tractography, the vector field $\boldsymbol{v}$ chosen to reflect the local fiber orientations that are calculated from the diffusion data.

To apply this equation in fiber tractography, the vector $\boldsymbol{v}$ is chosen to be the propagation direction, depending on the reconstruction technique used for tracking for DTI $\boldsymbol{v}$ is the field of the first eigenvectors derived from the diffusion tensor [64], in multiple fiber $\boldsymbol{v}$ consists of dDOF or fODF in order to make it general we call it the propagation direction. Note that Eq. (3.1) is a differential equation that can be solved by means of integration:

$$p(s) = p(s_0) + \int_0^t v[p(s)]ds \tag{3.2}$$

Where $p(s_0)$ is the starting point of the streamline which is referred to as a seed point now we can see that streamline tractography is the process of integrating through voxels pathways [12]. To begin tracking we need to initialize the starting seed points which have to be constrained by the volume's dimensions, we can choose them randomly or we can specify them explicitly [61, 12]. To perform the integration numerically we have to approximate the integration.

The easiest way for calculating the integration numerically is to use the Euler method. We divide the interval $[s_0, s_0 + \alpha]$ into N different part each of length $\Delta s = \frac{\alpha}{N}$ so that the point

$$s_k = s_0 + k\Delta s \tag{3.3}$$

Integrating our differential equation from p_k to p_{k+1} to get:

$$\int_{s_k}^{s_{k+1}} \frac{d\boldsymbol{p}(s)}{ds} ds = \int_{s_k}^{s_{k+1}} \boldsymbol{v}[\boldsymbol{p}(s)]\, ds \tag{3.4}$$

$$\boldsymbol{p}(s_{k+1}) = \boldsymbol{p}(s_k) + \int_{s_k}^{s_{k+1}} \boldsymbol{v}[\boldsymbol{p}(s)]\, ds \tag{3.5}$$

But since $s_k = s_0 + k\Delta s$ this is the same as;

$$\boldsymbol{p}(s_{k+1}) = \boldsymbol{p}(s_k) + \int_{s_k}^{s_k+\Delta s} \boldsymbol{v}[\boldsymbol{p}(s)]\, ds \tag{3.6}$$

If p_k is our approximation of $\boldsymbol{p}(s_k)$ then this gives rise to the scheme

$$\boldsymbol{p}_{k+1} = \boldsymbol{p}_k + \int_{s_k}^{s_k+\Delta s} \boldsymbol{v}[\boldsymbol{p}(s)]\, ds \tag{3.7}$$

It remain to find a way to estimate the area under the function $\boldsymbol{v}[\boldsymbol{p}(s)]$ on the interval $[s_k, s_k + \Delta s]$.One way we can approximate the integral

$$\int_{s_k}^{s_k+\Delta s} \boldsymbol{v}[\boldsymbol{p}(s)]\, ds \tag{3.8}$$

is by finding the area of a rectangle with height determined by the value of $\boldsymbol{v}$ at s = s_k (the left endpoint) and width Δs. In other words

$$\int_{s_k}^{s_k+\Delta s} \boldsymbol{v}[\boldsymbol{p}(s)]\, ds \approx \Delta s \boldsymbol{v}[\boldsymbol{p}(s_k)] \approx \Delta s \boldsymbol{v}[\boldsymbol{p_k}] \tag{3.9}$$

Substituting this approximation of the integral back into equation (3.1) gives the scheme

$$\boldsymbol{p}_{k+1} = \boldsymbol{p_k} + \Delta s \boldsymbol{v}[\boldsymbol{p_k}] \tag{3.10}$$

Which is just Euler's Method [65].

Euler method is good for fast tracking but since the error is big in this method accumulating the errors lead us to deviation from our streamline and propagate toward different direction rather than the actual propagation.

The sequence of the values $\boldsymbol{p}_1 \ldots \boldsymbol{p}_k$ obtained using Euler's method generally do not agree with the exact solution at each s_k,This is because the algorithm gives a straight-line approximation to the solution which yield an error, this error occurs at each step and is called the local truncation error [66], which depends on the step size chosen so if the step size is so small the error will be small but by decreasing the step size we need more steps, to find a good approximation another problem is that each time we calculate the next value which depend on an approximate value, this leads us to a global truncation error [66] which may lead to changing the direction of our streamlines.

The local truncation error in the Euler formula is $O(\Delta s^2)$ and the global truncation error is $O(\Delta s)$ for a better approximation we try to approximate the integration using approximation by trapezoids [67].

A more accurate way of approximating the integral

$$\int_{s_k}^{s_k+\Delta s} \boldsymbol{v}[\boldsymbol{p}(s)]\, ds \tag{3.11}$$

Is by finding the area of a trapezoid obtained by joining the points $(s_k, \boldsymbol{v}[s_k, \boldsymbol{p_k}])$ and the point $(s_k, \boldsymbol{v}[s_{k+1}, \boldsymbol{p_{k+1}}])$ by a straight line, and taking the area under this line segment. Using the formula for the area of a trapezoid, this area is:

$$\frac{\Delta s}{2}\left[\boldsymbol{v}[s_{k+1}, \boldsymbol{p_{k+1}}] + \boldsymbol{v}[s_k, \boldsymbol{p_k}]\right] \tag{3.12}$$

Substituting this area approximation for the integral in formula (3.1) gives:

$$\boldsymbol{p}_{k+1} = \boldsymbol{p_k} + \frac{\Delta s}{2}\left[\boldsymbol{v}[s_k, \boldsymbol{p_k}] + \boldsymbol{v}[s_{k+1}, \boldsymbol{p_{k+1}}]\right] \tag{3.13}$$

The problem with this scheme is that we cannot use it to find $\boldsymbol{p}_{k+1}$ in its current form, because appears on the right side of this equation, inside the function $\boldsymbol{v}$ **,** to deal with this issue, we will approximate the $\boldsymbol{p_{k+1}}$ appearing inside $\boldsymbol{v}$ with the approximation given by Euler's method. That is, on the Right hand side we can approximate $\boldsymbol{p}_{k+1}$ with:

$$\boldsymbol{p}_{k+1} = \boldsymbol{p_k} + \Delta s \boldsymbol{v}[\boldsymbol{p_k}] \tag{3.14}$$

And $s_{k+1} = s_k + \Delta s$ to get the scheme:

$$\boldsymbol{p}_{k+1} = \boldsymbol{p_k} + \frac{\Delta s}{2}\left[\boldsymbol{v}[s_k, \boldsymbol{p_k}] + \boldsymbol{v}\left[s_k + \Delta s, \boldsymbol{p_k} + \Delta s \boldsymbol{v}[\boldsymbol{p_k}]\right]\right] \tag{3.15}$$

Starting with the initial condition and using this formula to successively find the values known as the improved Euler's [68] also known as Heun's method, it looks a bit complicated. We would actually compute it in three steps [69]:

$$m_1 = \boldsymbol{v}[\boldsymbol{p_k}] \tag{3.16}$$

$$m_2 = \boldsymbol{v}\left[s_k + \Delta s, \boldsymbol{p_k} + \Delta s \boldsymbol{v}[\boldsymbol{p_k}]\right] \tag{3.17}$$

$$\boldsymbol{p}_{k+1} = \boldsymbol{p_k} + \frac{\Delta s}{2}[m_1 + m_2] \tag{3.18}$$

The local truncation error for the improved formula is $O(\Delta s^3)$ as opposed to $O(\Delta s^2)$ for the Euler's method. It can also be shown that for a finite interval, the global truncation error for the improved Euler formula is bounded by $O(\Delta s^2)$, by this we can say that the Improved Euler method is of second order [70].As we can see closely that the improved Euler formula uses the Euler formula in our algorithm we use Improved Euler for propagating trough streamlines, from the equation 3.17 to calculate m_2 we need to calculate first the Euler approximation, which is a needed step so if we save the value of the Euler method as:

$$\boldsymbol{eu} = \boldsymbol{p_k} + \Delta s \boldsymbol{v}[\boldsymbol{p_k}] \tag{3.19}$$

After that we calculate $\boldsymbol{p}_{k+1}$ as described above, subtracting the **eu** from $\boldsymbol{p}_{k+1}$ yield to a calculation error

$$e = \boldsymbol{p}_{k+1} - \boldsymbol{eu} \tag{3.20}$$

$$e = \frac{\Delta s}{2}\left[\boldsymbol{v}\left[s_k + \Delta s, \boldsymbol{p_k} + \Delta s \boldsymbol{v}[\boldsymbol{p_k}]\right] - \frac{1}{2}\boldsymbol{v}[\boldsymbol{p_k}]\right] \tag{3.21}$$

Since the points $\boldsymbol{p_k}$are in 3D we calculate the error in three axis x, y and z

$$\Delta\vec{s} = \vec{\imath}\Delta x + \vec{\jmath}\Delta y + \vec{k}\Delta z \tag{3.22}$$

So that:

$$e_x = \frac{\Delta x}{2}\left[\boldsymbol{v}\left[x_k + \Delta x, \boldsymbol{p_{x,k}} + \Delta x \boldsymbol{v}[\boldsymbol{p_{x,k}}]\right] - \frac{1}{2}\boldsymbol{v}[\boldsymbol{p_{x,k}}]\right] \tag{3.23}$$

$$e_y = \frac{\Delta y}{2}\left[\boldsymbol{v}\left[y_k + \Delta y, \boldsymbol{p_{y,k}} + \Delta y \boldsymbol{v}[\boldsymbol{p_{y,k}}]\right] - \frac{1}{2}\boldsymbol{v}[\boldsymbol{p_{y,k}}]\right] \tag{3.24}$$

$$e_z = \frac{\Delta z}{2}\left[\boldsymbol{v}\left[z_k + \Delta z, \boldsymbol{p_{z,k}} + \Delta z \boldsymbol{v}[\boldsymbol{p_{z,k}}]\right] - \frac{1}{2}\boldsymbol{v}[\boldsymbol{p_{z,k}}]\right] \tag{3.25}$$

To calculate the error between these methods we calculate the length.

$$e = \sqrt{{e_x}^2 + {e_y}^2 + {e_z}^2} \tag{3.26}$$

If the step size is too small this error will decay to zero whereas for bigger step size the error will decrease and the difference error will grow rapidly which means our approximation is not good enough, to minimize the error more we are going to use another method called Range-Kutta [71].

Range-Kutta is one of the well known high order approximation method. It is used in this work for fiber tracking as follows:

$$\boldsymbol{p}_{k+1} = \boldsymbol{p_k} + \frac{1}{6}\left(\boldsymbol{K}_1 + 2\boldsymbol{K}_2 + 2\boldsymbol{K}_3 + \boldsymbol{K_4}\right) \tag{3.27}$$

Where:

$$\boldsymbol{K_1} = \boldsymbol{v}[\boldsymbol{p_k}]\Delta s \tag{3.28}$$

$$\boldsymbol{K_2} = \boldsymbol{v}\left[\boldsymbol{p_k} + \frac{\boldsymbol{K_1}}{\boldsymbol{2}}\right]\Delta s \tag{3.29}$$

$$\boldsymbol{K_3} = \boldsymbol{v}\left[\boldsymbol{p_k} + \frac{\boldsymbol{K_2}}{\boldsymbol{2}}\right]\Delta s \tag{3.30}$$

$$\boldsymbol{K_4} = \boldsymbol{v}[\boldsymbol{p_k} + \boldsymbol{K_3}]\Delta s \tag{3.31}$$

The RK4 scheme has an associated error of order $O(\Delta^5)$ and it is known to be a good candidate for the numerical solution of Eq. (3.2).

The problem with Range-kutta method is the number of steps it needs to perform the calculations, which is the case of the brain fibers. Since the brain has millions of fiber connections, if we want to visualize a large set of data, we will take more time to get the results rather than using improved Euler, which is fast with small error. In this work, we are going to use the two methods Improved Euler and Range-Kutta fourth order. Combining the two approaches in one algorithm is a bit tricky, we use the error calculated in Eq. (3.26) and introduce a threshold error as a checking criteria.

Since the integration, using the Euler method uses step size to approximate the next propagation direction. If the error distance between the points approximated using Improved Euler and the point approximated using Euler is less than the threshold error value, in this case we are sure that our approximation is not good enough. We would have to approximate more using RK4, since our calculation of the Improved Euler method needs to use Euler approximation, the calculation of the error will be straight forward after calculating the $\boldsymbol{p}_{k+1}$point.

To test our approximation we assume that the fourth order Range-kutta is the nearest approximation to the real solution, using this assumption we calculate the error difference between the Range-Kutta and Euler and between the Improved Euler and the Range- Kutta:

$$e_{ImprovedEuler,Euler} = \left|p_{ImprovedEuler} - p_{Euler}\right| \tag{3.32}$$

$$e_{RK4,Euler} = \left|p_{RK4} - p_{Euler}\right| \tag{3.33}$$

$$e_{RK4,ImprovedEuler} = \left|p_{RK4} - p_{ImprovedEuler}\right| \tag{3.34}$$

Using step size as 0.5, we get the following results:

Table 3.1: *Error calculation in three different tracks*

Seed points	$e_{ImprovedEuler\ ,Euler}$	$e_{RK4\ ,ImprovedEuler}$	$e_{RK4\ ,Euler}$
Track 1	0.0576195612863	0.0019546869365	0.0560742444035
	0.0557849966691	0.0121300687036	0.0676890993319
	0.0511924468404	0.0148377528737	0.0367217369928
	0.178773312811	0.0639262604132	0.228885003534
	0.102375791345	0.017998658162	0.116767687278
	0.0757052460983	0.0112006884788	0.0864092983055
	0.0865655081301	0.00644890009632	0.0881453360272
Track 2	0.15415272309	0.00938398944952	0.145067600414
	0.0503284059792	0.00260485519114	0.0499633589229
	0.0589351532547	0.00495295373072	0.054635883389
	0.0927663068447	0.0167723549338	0.108785865663
	0.0548818206792	0.0112023585569	0.0499222085905
	0.0544288010299	0.00855136074335	0.0573666269158
	0.0651257770491	0.0106441185884	0.0665637425526
Track 3	0.0539418678609	0.0133096014242	0.0611826844786
	0.0523046570513	0.00484389236917	0.0483245694051
	0.0990173268704	0.0573339981335	0.156165118255
	0.0523578743127	0.00697790715592	0.0467430473215
	0.054190791841	0.0214855753206	0.0756490762736
	0.0574221431078	0.00240209396082	0.0577694390745
	0.0513371650034	0.0126426296502	0.0389949214527
	0.0665907048694	0.00387158825423	0.0689115533048

As we can see in table 3.1, the error calculation between RK4 and Improved Euler is smaller than the one between RK4 and Euler. In most cases this error is less than 10 % of the step size, which lead us to use the Improved Euler for calculation and going for a fourth order Range-kutta if this error is more than 10%. We call this error the threshold difference error.

Also, we notice from table 3.1 the error between RK4 and Euler is more than 10% of the step size, which may lead us to a wrong approximation of the track, and if the error accumulate in this way it may lead us to a totally wrong fiber track. We compare our error to the step size rather than any other calculation in order to make it valid for different step size.

Using different step size could decrease the error but the problem with that is the time complexity is inversely proportional to the step size another factor is when using smaller step size generate a lot of tracking points which may depend on the hardware used for it.

In order to stop the propagation two criteria are commonly used a threshold on the diffusion anisotropy and an angular threshold, these thresholds differ from reconstruction algorithm to another. The well-known DTI tractography is common to stop when FA is below certain value (typically FA < 0.2) [12], this is because the region of low FA tends to have high uncertainty in the principal diffusion direction. When dealing with multi-fiber reconstruction algorithms we usually finish tracking when the dODF or fODF amplitudes along the current tracking orientation fall below a certain threshold. All this functions try to measure anisotropy in every single voxel this measure have to be greater than zero everywhere in the volume.

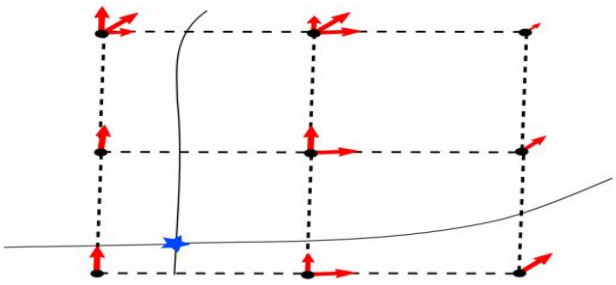

Figure 3.1*: In every voxel centre (black dot) there are one or more vectors. These vectors represent peaks where their length is equal to their anisotropy value and the direction is equal to the direction of the peake.g. calculated from a given ODF. Eudx as well as CIERTE can track multiple peaks starting from a single seed point (star) if their anisotropy values are higher than a threshold. In that way we can track from the same seed towards different directions and support tracking in crossing areas as it is shown here [61].*

For simplicity, we represent all these measures with a function F. Therefore, when we write $F(u_i) = \alpha_i$ this will read for the peak unit direction u_i the peak value is α_i for FA this will be the eigenvector corresponding to the highest eigenvalue [61,64].:

$$F(e) = FA \tag{3.35}$$

For multiple peaks like QA, which allow any number of peaks we use $F(u_i) = QA_i$ we constrain it to five peaks in our algorithm. The concept of tracking with the combination of multiple peaks is shown in Figure 3.1. By replacing the vector u by the closest vertex of an evenly distributed and dense of unit sphere allows as to reduce the storing space and by estimating F(u_i) at every point of the volume which represent a composite vector field where every point contains the peak direction superimposed to the anisotropy value.

In order to count the tracks we create an empty list of tracks $= \emptyset$, the first point to be appended is the starting point or the initial point, ones we have our initial seed point we are ready to propagate. The propagation will be in two directions the forward and backward, when we finish with one track we need to propagate toward another track until we finish all the tracks. We propagate toward the opposite direction, which can help us detect the crossing area; this will be useful especially when we combine it with the information of the function F, as it is common with QA.

We need to check where we stop tracking, our algorithm check for a maximum threshold value so that $F(p_n) < F_{thr}$ if this is not the case we append the point to the list and continue tracking. Checking for F_{thr} could be useful especially when we have low anisotropy areas where we do not need tracks, F_{thr} depends on the reconstruction method and it will give us different results if we keep the same threshold value.

In order to generate a smooth tractography, it is recommended to use some kind of interpolation; this is in contrast with FACT, which does not use neighboring information. The fiber orientations are available at arbitrary positions in space. Unfortunately, the diffusion data that the local fiber orientations derived from acquired on a rectangular imaging grid. Therefore, we need a method for interpolating the discrete measurements into continuous space. The simplest method to obtain an estimate of the local fiber orientation at any location is to use nearest-neighbor interpolation [72].

The contribution from each neighboring point result in fiber orientation between grid points assume to have contribution from other points .The neighboring points are the points which have great contribution to the fiber orientations. Trilinear interpolation is the mostly used interpolation technique, where the quantity of interest is calculated as a weighted sum from the eight nearest voxels nearest to the point of interest.

We use trilinear interpolation for predicting the next direction only. The seed point divides the neighboring area in eight regions in 3D space we add the weights w of the antipodal side this weight is a sub volume in 3D the trilinear interpolation gives us the weight

corresponding to each direction, which define the peaks of the neighboring voxels, which will assign the next direction.

We describe here how we use the trilinear interpolation weights with the CIERTE algorithm in order to find the next propagation direction.

a) Starting from the initial direction, we find the nearest direction $\boldsymbol{v(p_n)}$ to every peak direction $\boldsymbol{u_i}$of every one of the eight corners of the neighborhood of the seed.
b) Checking for the threshold value. If $arccos(x_i, p_n) <= \boldsymbol{\theta_{thr}}$ we count the corresponding weight; otherwise we continue to the next weight.
c) Simultaneously check for the condition of the anisotropy threshold:

$$F(u) \leq F_{thr}(\mathrm{u}) \tag{3.36}$$

All the adjacent weights will contribute to the new direction according to the following formula:

$$v'(p_n) = \sum_m w_m \, v(p_m) \tag{3.37}$$

Where $v(p_m) = \frac{v'(p_n)}{|v'(p_n)|}$ is normalized.

d) The next point is calculated with Eq.3.14 if the error less than the threshold error Eq (2.26) otherwise, it will be calculate using Eqs 3.27, 3.28, 3.29 and 3.31.

e) If the error in Eq 3.26 is small than the error threshold we approximate more using rang Kutta in equation 3.27.

f) We insert the new point in the track and continue tracking until one of the stopping criteria is met. The next step will be to repeat the *a-f steps* for the opposite direction of the initial peak direction v(p_0)a as described above.

Finally, we will have to repeat the procedure for the next seed point until all seed points are visited. When all seeds have been visited, we will have in our hands the entire tractography. A description of CIERTE is given in Algorithm 1, 2 and 3.

Apart from the anisotropic threshold F_{thr} and angular threshold$\boldsymbol{\theta_{thr}}$, other anisotropic criteria are also incorporated in CIERTE. These are:

a) The total sum of weights TW, which helps us in edge corners where the tracking should stop the total weight checks if there is enough overall neighboring contribution to continue tracking (default value of 0.5) [61].

b) We limit the track points to a certain number in order to avoid the divergence of the track, because it is possible for a track to get trapped in a loop and start looping forever. We can check for maximum number of points describing a track MNP (default maximum value 1000 points).

c) We need finally to check that our track is bounded by the volume shape, the 3D volume is held in a variable V.

Algorithm 1 CIERTE

Input F, I, S, V, U, TW, MNP
Δs ,F_{thr},θ_{thr},e_{thr}
Output T

$T \leftarrow \emptyset$

For seed in S Do
    For peak in (F, I) Do
    $Track \leftarrow CIERTE\_Core\_Alg(seed,peak)$
    Append(T,track)
    EndFor
EndFor

Algorithm 2 CIERTE_Core_Alg

Input Seed,Peack, $\Delta s, V, e_{thr}$
Output Track
$Track \leftarrow \emptyset$
delta, i_direction←Initial_Direction(seed)
#propagate orthograde (forward direction)
direction← i_direction
While delta is True Do
    delta, n_direction← New_Direction(direction)
        If delta is False Do
            Break
        EndIf
        *tmp1 ←point + Δs*n_direction*
        tmp2 ←New_Direction(tmp1)
    point← point + $\frac{\Delta s}{2}$ *(n_direction + tmp2)*
        error = abs(point – tmp1)
        If error >e_{thr}
        delta ,tmp← RK4_Alg(seed,peak)
            If delta is True
            Point ← tmp
            EndIf
        EndIf
        append(track,point)
        direction← n_direction
    EndWhile
    delta←True
    #propagate retrograde(toward the opposite #direction)
    direction← - i_direction
    While delta is True Do
        #Same as above

Algorithm 3 RK4_Alg

Input Seed,Peack,point, Δs*,V,*
Output tmpn_direction,delta
delta, n_direction← *New_Direction(direction)*
k1 ← *n_direction* * Δs
If delta is True
delta, K2 ←*New_Direction(direction* + $\frac{k1}{2}$*)*∗ Δs
Else
Delta ←*False*
EndIf
If delta is True
delta, K3 ←*New_Direction(direction* + $\frac{k2}{2}$*)*∗ Δs
Else
Delta ←*False*
EndIf
If delta is True
delta, K4 ←New_Direction(direction + $k3$)∗ Δs
Else
Delta ←*False*
EndIf
If delta is True
tmp← point +$\frac{1}{2}(k1 + \frac{K2}{2} + \frac{K3}{2} + K4)$
n_direction←K4
Else
Delta ←*False*
EndIf

We apply algorithm 1 to all tractography, as an input to algorithm 1 F represent the 4D volume that represent the peaks $\boldsymbol{I}$ represent the index direction of the 4 dimensional volume of each peak in relation to the unit sphere U. U is an array of size N X 3 where N is the number of vertices in the sphere, the seed points are represented by a 3D array, Δ**s** is the propagation step size.

$\boldsymbol{F_{thr}}$**,** defines the lowest possible peak value that allows tracking to continue. $\boldsymbol{\theta_{thr}}$**,** is the maximum allowed angle between the current propagation direction and the next direction. TW checks the overall contribution of the neighborhood for the next propagation direction and MNP checks that a track does not pass from the same point more than a number of times MNP [61].

$\boldsymbol{e_{thr}}$is the error threshold which tell us either to go approximate more or continue tracking with Improved Euler, *V* represent the volume.

Only variable $\boldsymbol{F}, \boldsymbol{I}, \boldsymbol{S}, \boldsymbol{V}$ have to be updated each time we repeat the track the other parameters are steel the same.

The core algorithm is given in algorithm 2 and 3 in order to know that the propagation is in the correct direction we check for a return value delta [61] if this value is true we continue the procedure if the value is false we stop tracking and move to the next track.

The thing that is new in our algorithm is the calculation of the error, which will be compared to the threshold error; we set a default value of 10% of the step size as a threshold error given in the beginning of the track. We use this error to check the accuracy of the approximated value if this value is not accurate enough. Then we would have to approximate using RK4 in algorithm 3, which is believed to be one of the best approximation. We check the delta function in both algorithm 2 and 3 to be sure we do not have wrong value, and if a stop criteria occurs in any of the algorithms and does not occurs in others we make sure the tracking continue without problem. By checking in every step the delta function we then repeat algorithm 1 for each seed point and append the calculated point to the track when we have a stopping criteria we append the track to the total track. We set the delta function to be true and continue tracking toward the opposite direction do the same procedure for every track until we have the full tractography.

3.3 EXPERIMENTAL RESULTS:

In order to test our algorithm we have used Stanford HARDI [73] data set of a real human brain, we apply our algorithm on three different reconstruction methods DTI for single orientation and for high order, we use Q-ball images. Also to test the crossing fiber assumption we use CSD method we use 50000 seed points as a limit with 0.2 threshold for FA for DTI, and 0.2 GFA threshold for Q-ball and FA=0.88 for CSD we use 10% of step size threshold error difference with a step size of 0.5. As we can see in the Figure 3.2 the difference between the tractography algorithms used for the three reconstruction methods CSD, Q-ball and DTI. The threshold value of FA varies from one technique to another this is why we did not use the same FA threshold in the three different methods. We use different values of the low threshold to see how this affects the track, which gives you area where we do not need tracking like CSF.

CIERTE can deal with multiple crossing regions, which is the case of multiple ODF reconstruction methods, we use CSD as a high order and efficient method to visualize this crossing criteria we use a threshold for FA to be 0.7 with step size of 0.5 and 50000 seed points we visualize the data in Figure 3.4.

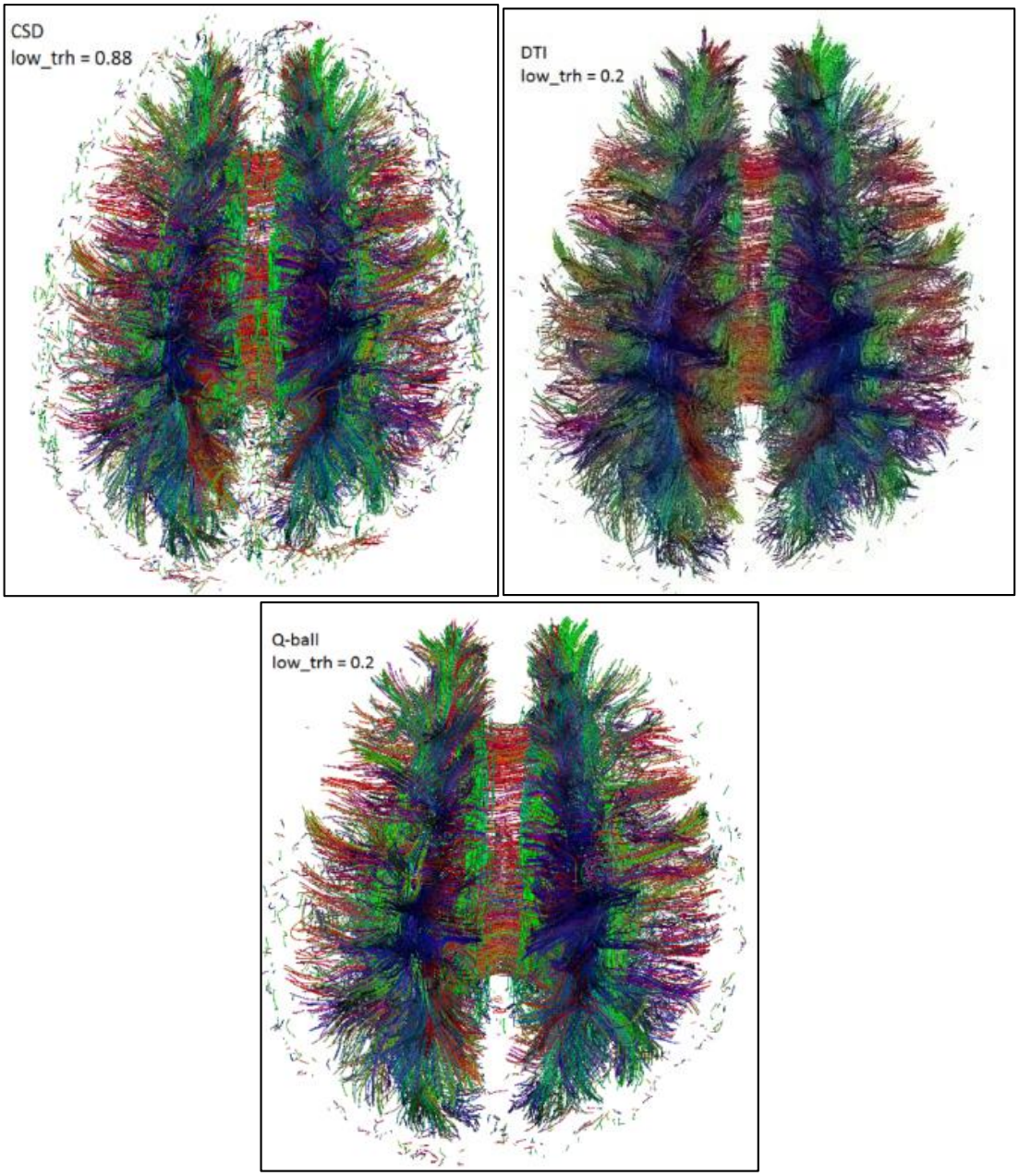

Figure 3.2*: Tractography using CIERTE algorithm for CSD, DTI and QBI using low Anisotropy threshold of 0.88, 0.2 and 0.2 respectively*

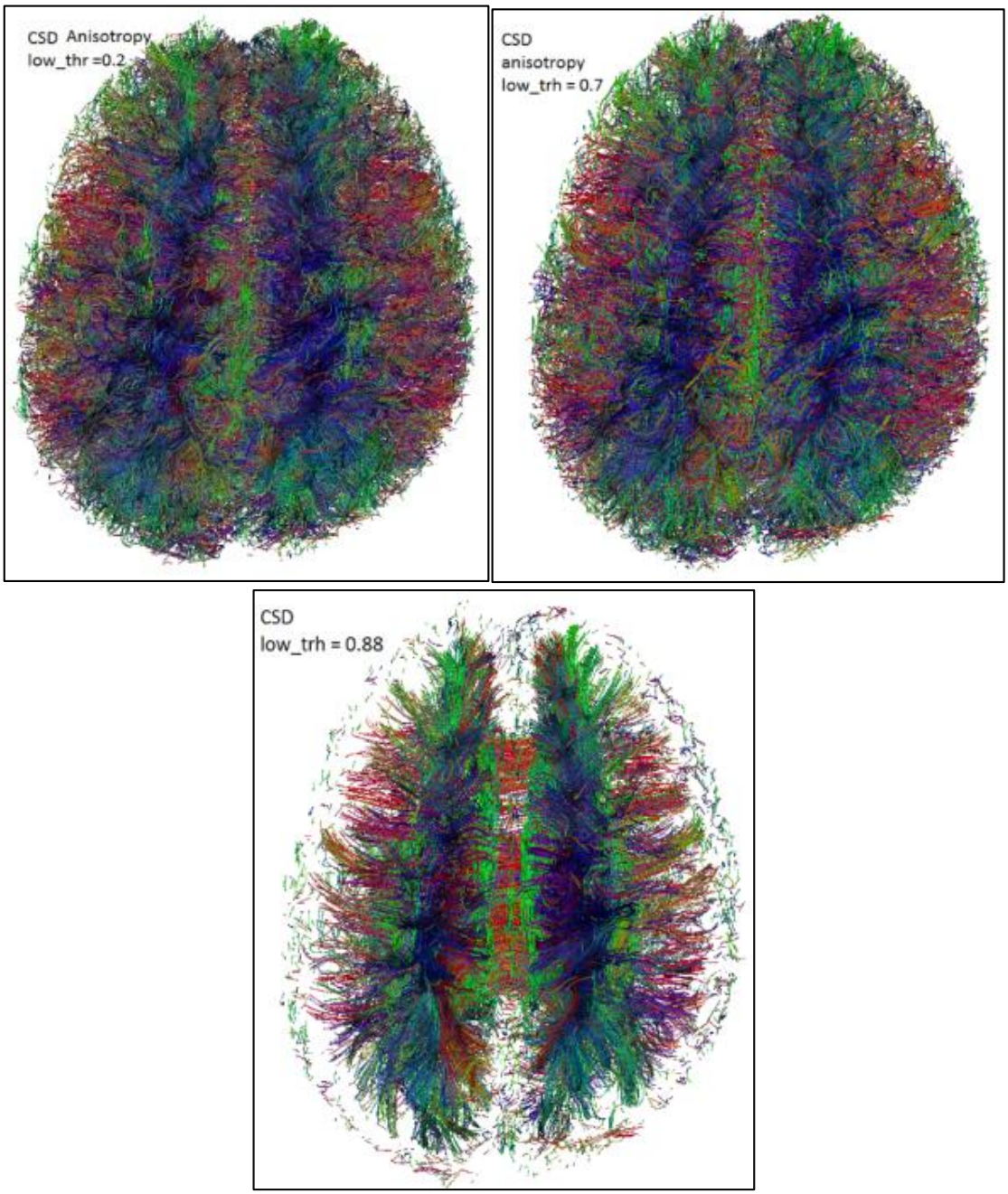

Figure 3.3*: The effect of changing the low Anisotropy threshold in the CSD model using 0.2, 0.7 and 0.88 respectively*

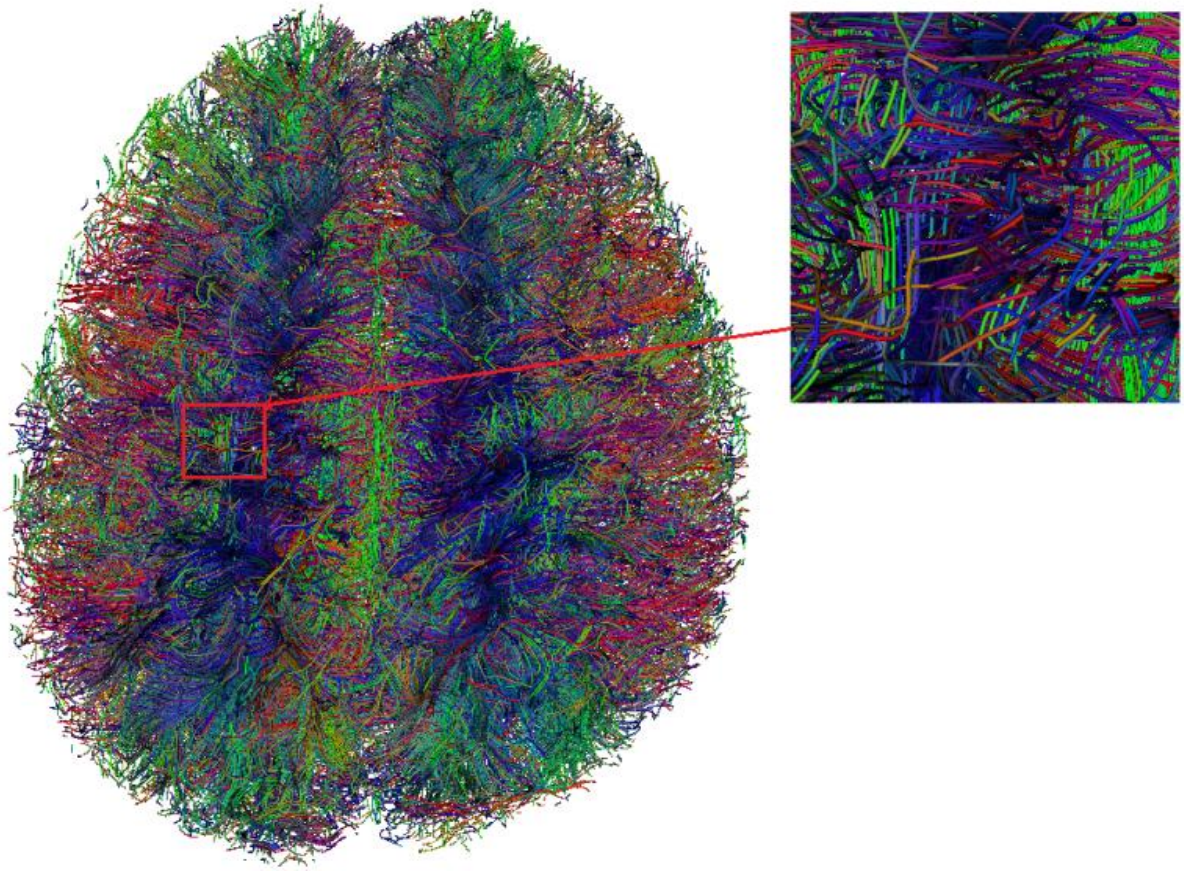

Figure 3.4*: Multiple crossing fibers Using CSD model as a reconstruction technique.*

We use CSD with anisotropy measures below 0.88 threshold value and 0.5step size. We visualize ½ million seed points and calculate the tractography of the brain. We are interested in area in the corpus coliseum, in order to make the visualization quick we use lines instead of tube for visualizing the fibers you can see the result in Figure 3.5.

All the algorithms and visualizations are implemented in our software DIVIZ, which is described in our LICENCE degree project [74], we did not go in details into DIVIZ because it is out of the scope of this work and it is well documented in our LICENCE project, the tractography results using DIVIZ are shown in Figure 3.6

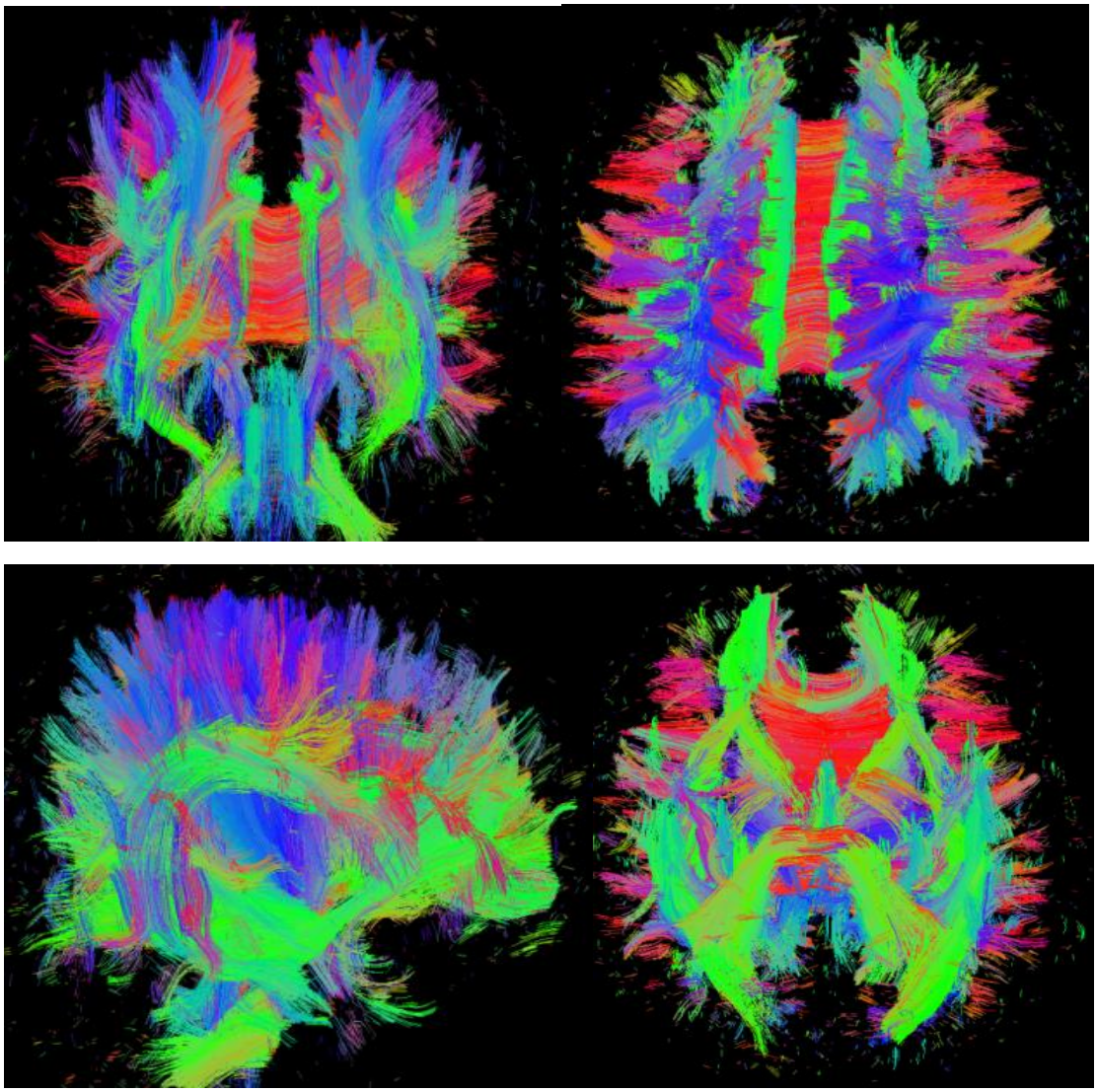

Figure 3.5*: Tractography of the brain using 500000 seed points and 0.5 step size with CSD model by tacking the low anisotropy threshold to be 0.88 using CIERTE algorithm*

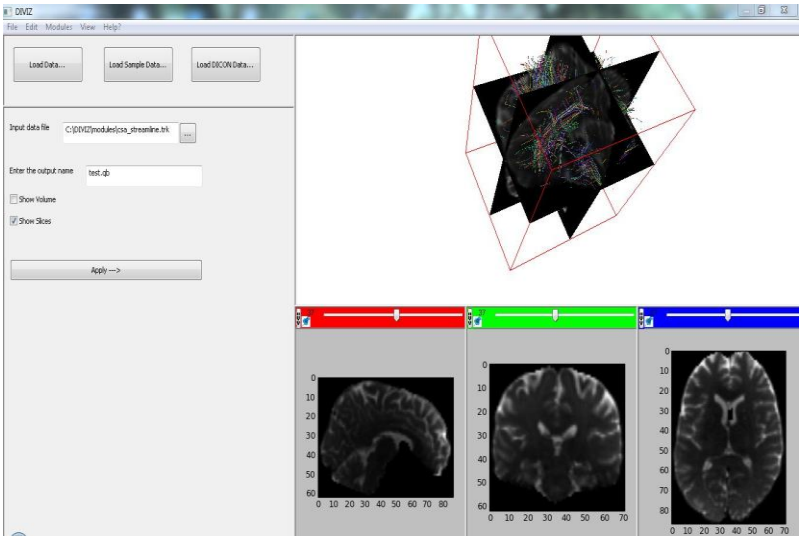

Figure 3.6 :*an overview of our DIVIZ software when visualizing tractography.*

As a result of determinsitc tractography based on Q-ball (constant solid angle) reconstruction techniques we take multiple view point and illustrate some visualizations in the results of the visualisation using our software is shown in Figures 3.7.

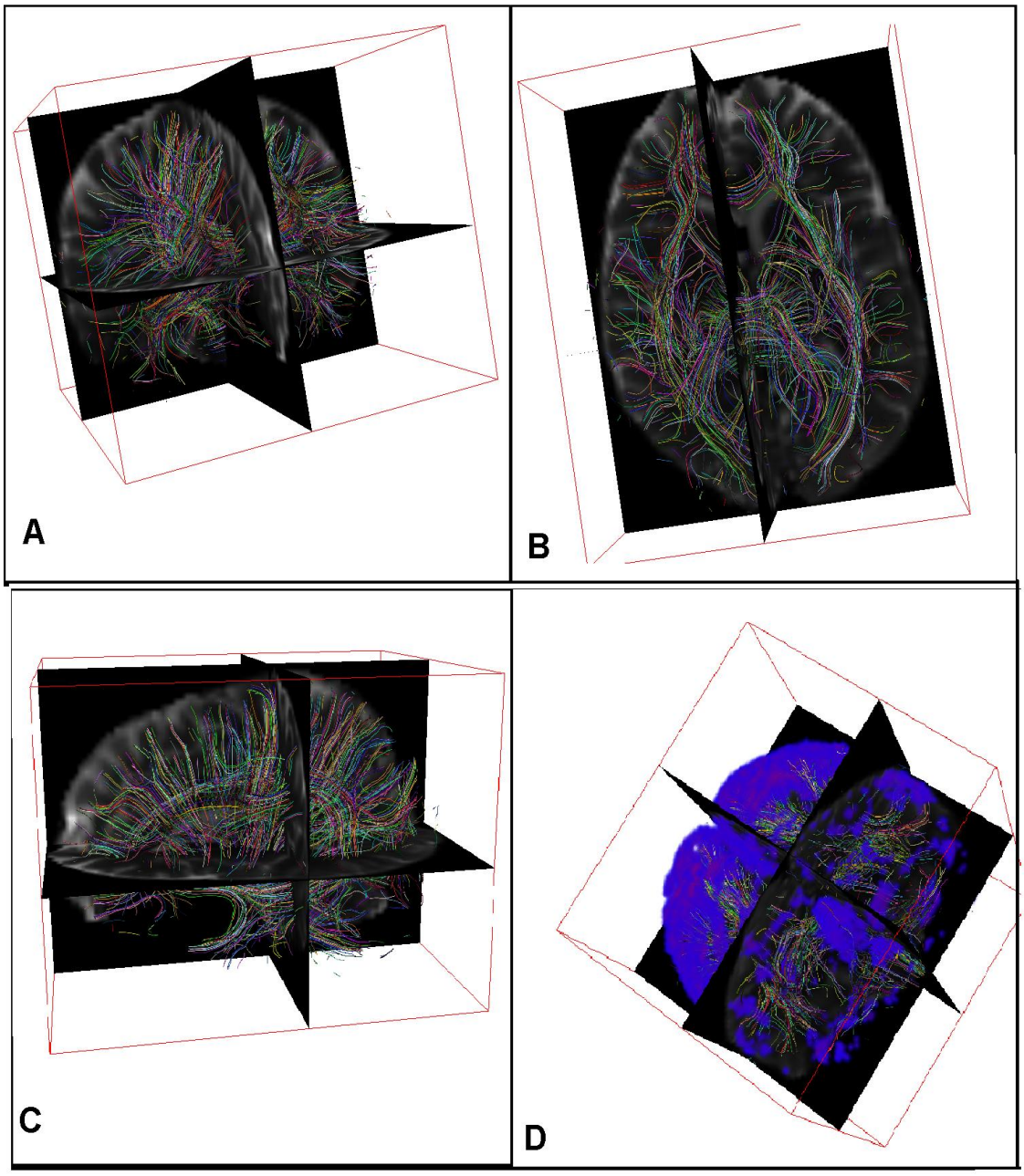

Figure3.7 : *Deterministic tractography visualized using DIVIZ from different view angels*

In Figure 3.7 we show the Deterministic tractography visualized using DIVIZ from different view angels, for A, B and C and visualizing the volume of the brain with tractography for better view for the bundles position.

3.4 Effects of changing the step size:

One of the limitations is the step size. We have calculate for three different step size and we visualize the tracks to see how the step size could affect the tractography, Figure 3.8 illustrate the step size problem as step size increase the error grow and the tracks will behave differently.

Another thing which is worth nothing is the number of seed points that we can visualize, it is important because the brain is composed of millions of fibers if one could approximate some of this fibers and do tracking along we could obtain good approximation of the brain structure.

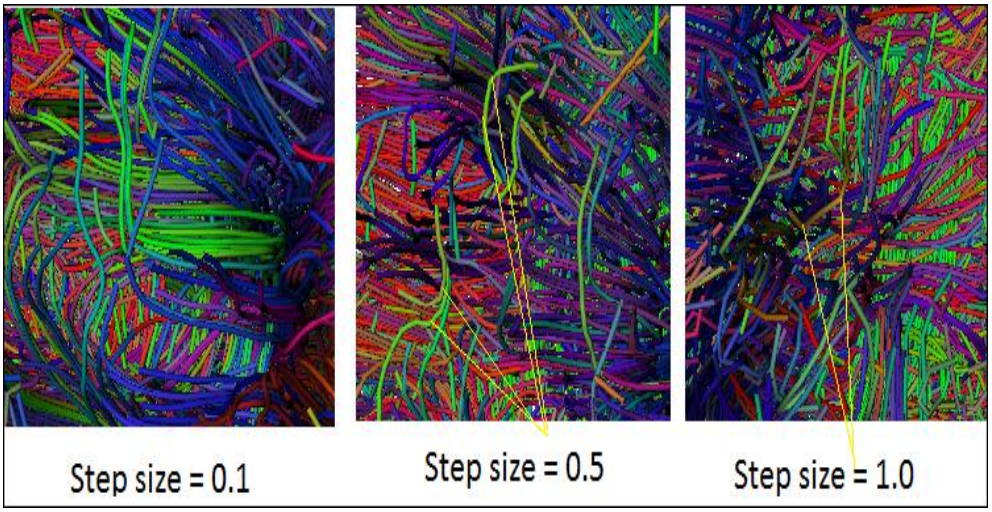

Figure 3.8*: The effect of changing the step size on the fiber tracks*

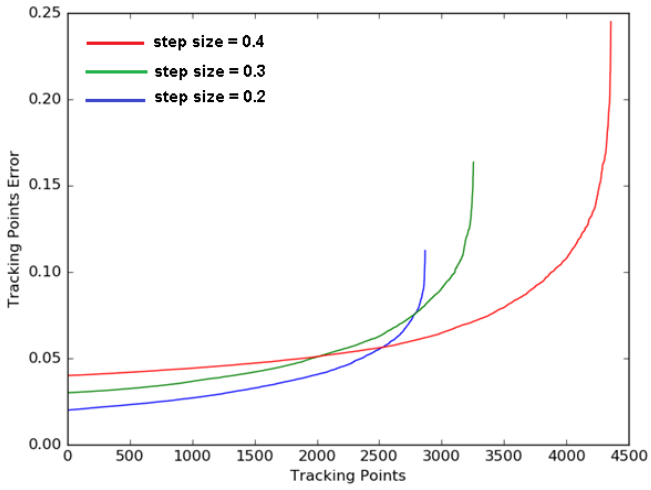

Figure 3.9*: The tracking point error values/numbers relation with different step-sizes.*

In Figure 3.9, we can see that each time we increase the step size, the number of erroneous tracking points increases (as we see in the Figure 3.9; at step size=0.2,0.3 and 0.4, the number of false tracking points is 2869, 3257 and 4359 points respectively). Another thing to observe is that we have about 2500 false points with an error below 0.05mm for the three step sizes. This value is small enough to be considered as a minimum threshold error which, led us to minimize the use of Range-Kutta forth order approximation. The graph is rising exponentially meaning that we do not have many false points near the maximum error value and that the number of those points increases as the step size increases.

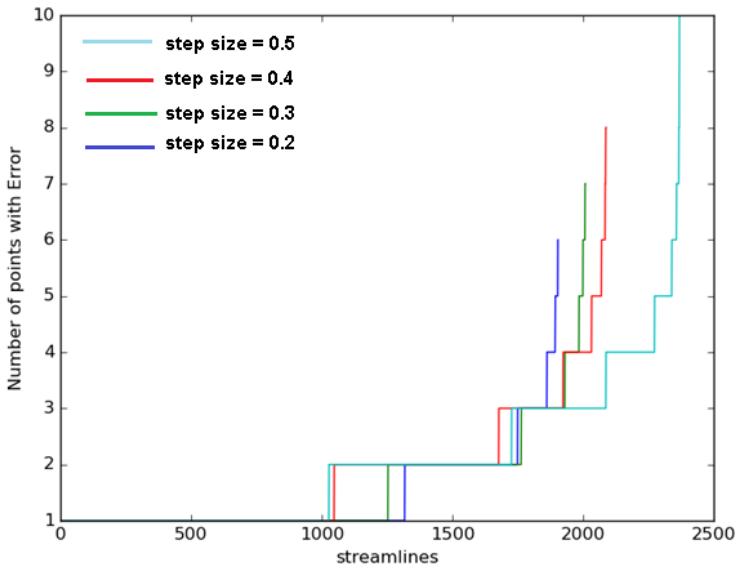

Figure 3.10*: The number of erroneous tracking points in affected streamlines for different step-sizes (0.2, 0.3, 0.4 and 0.5).*

We see in Figure 3.10 that the number of affected streamlines (a streamline contains at least one false tracking point) increases as the step size do so. Also, within each affected streamline the number of false points rises proportionally with the step size.

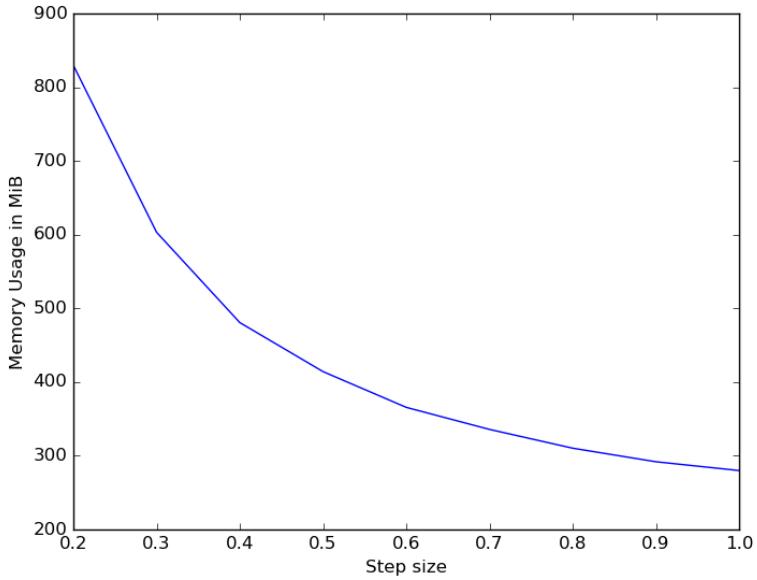

Figure 3.11: *memory usage (RAM) versus step-size.*

We clearly see from Figure 3.11 that the memory usage and the step size are inversely proportional.

We deduce from these three last Figures 3.9, 3.10 and 3.11 that if the selected step size is big, it could lead us to global truncation error. In the other hand, decreasing the step size produces more tracking points meaning more memory and processing time. So we have a trade-off to choose the step size carefully and a 0.2 is a good choice.

3.5 Summary:

Deterministic streamline tractography is subject to integration errors. It is important to realize that all these errors will accumulate along the streamline, which produce a global truncation error. We had focus our study on the effect of integrating error, many parameters put in the study, like step size and seed points. We try to make the fast, accurate and general tractography algorithm, so that the speed, accuracy, and hardware limitation are a concern and how this last affect the streamline more than any other parameter; we have seen the difference between reconstruction models and their effect.

CIERTE Evaluation Using Tractometer

In this chapter we are going to evaluate the CIERTE results using the Tractometer evaluation system in order to verify the validity of CIERTE algorithm and make a solid comparison with a state of the art tractography algorithm Eudx, we will also validate the conclusions we lead to in chapter 3 and see clearly the limitations of some algorithms.

4.1 Introduction:

In the past ten years, the diffusion community done a good work in the study and improvement of diffusion tensor imaging and its limitations. Numerous new tractography algorithms based on high angular resolution imaging (HARDI)[75] have been proposed, most of which have been tested quantitatively based on the accuracy of the orientation distribution function (ODF) and the sharpness of the peaks (angular resolution) ,and their reconstruction based on simulated data.

In neurosurgery, quantitative evaluation of fiber tracking results has been done by comparing tracts to electro cortical stimulation points [76], or by measuring patient outcomes given the use of Tractography for the resection of tumors[77][78].

Validation of fiber Tractography algorithms raise a challenge into developing new general tools for measuring the accuracy of the algorithms and how well the brain connectivity is established. Recently some evaluation systems use the publicly available FiberCup phantom datasets (www.lnao.fr/spip.php?article112), which is a dataset dedicated to the study of diffusion models [79] it was used for quantitative evaluation of tractography algorithms.

A new Evaluation tool have been introduced which is based on a revised FiberCup analysis that is closer in spirit to brain connectivity the name of this tool is tractometer [80].

In brain connectivity, the importance is connectivity. Does region A connect to B as expected? Does region A connect to unexpected regions of the brain? Therefore, instead of using local seeds and local point-by-point distances for evaluation, the Tractometer use a global view of the dataset and the fiber Tractography streamline output.

In this work, we are going to verify the CIERTE algorithm using the tractometer (http://www.tractometer.org/) evaluation system, in collaboration with Sherbrooke Connectivity Imaging Lab (Canada), and Inria Sophia Antipolis Mediterranean Research Institute (France) and obtain the tractometer evaluation parameters and results.

4.2 The Tractometer Evaluation System

The Tractometer is a tractography evaluation tool. It is used to evaluate the end effects on fiber tracts of different:

- acquisition parameters & artefacts (b-value, number of directions, denoising or not, averaging or not)
- local estimation & modeling techniques (tensor, q-ball, spherical deconvolution, spherical wavelets, compartment models)
- Tractography parameters (masking, seeding, stopping criteria)
- Tractography algorithms (deterministic, probabilistic, geodesics, global).

The tractometer has an evaluation method to compare Tractography pipeline streamline outputs and evaluate the number of found and not found fiber bundles, the proportion of streamlines part of existent and non-existent bundles, and the proportion of incomplete streamlines.

At this stage, a user has the choice of providing three things to the system:

- A diffusion dataset corrected with the user's best algorithm.
- A field of ODFs coming from the user's best algorithm.
- A set of streamlines.

The user can then obtain a ranking against the current database of state-of-the-art techniques.

The tractometer team performed a survey with neurosurgeons and neurologists at their institute concerning true and false connections, and false positives of streamlines; they concluded that these terms are not the best choices for connectivity analysis purposes. Therefore, they define the following six new terms [80]:

a) Average Bundle Coverage (ABC): the proportion of a fiber bundle covered by streamlines. ABC is reported in % (percentage) and is the average of the number of voxels crossed by streamlines divided by the total number of voxels in the bundle. For example, in Figure. 4.1, bundles 4, 6 and 7 have a high ABC, whereas bundle 3 has a much lower ABC.

b) Valid Connections (VC): streamlines connecting expected ROIs and not exiting the expected fiber bundle mask. This is illustrated by streamlines in Figure. 4.1 (right). VC will be reported in % of valid connections.

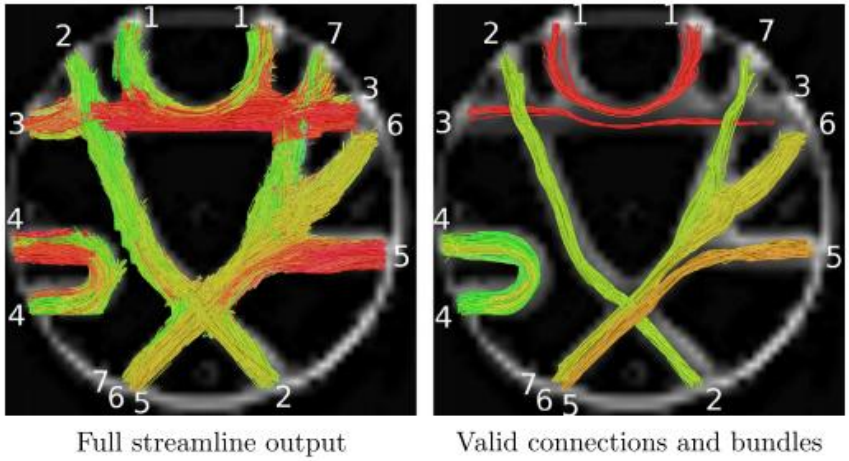

Figure 4.1. *Example of a tractography pipeline output and the resulting valid connections filtered by the ROIs [80].*

c) Invalid Connections (IC): streamlines connecting unexpected ROIs or streamlines connecting expected ROIs but exiting the expected fiber bundle mask. These streamlines are spatially coherent, have managed to connect ROIs, but do not agree with the ground truth (see Figure. 4.2).

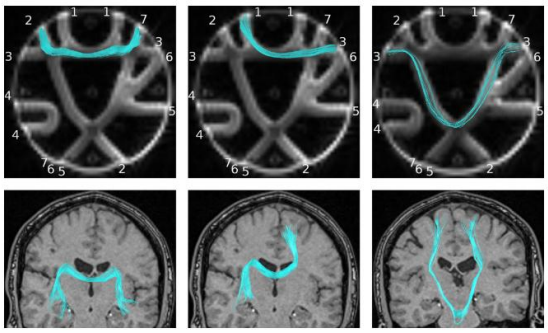

Figure 4.2 :*Invalid Connections (IC) between 2 ROIs of gray matter on the FiberCup and the real data analogies.[80]*

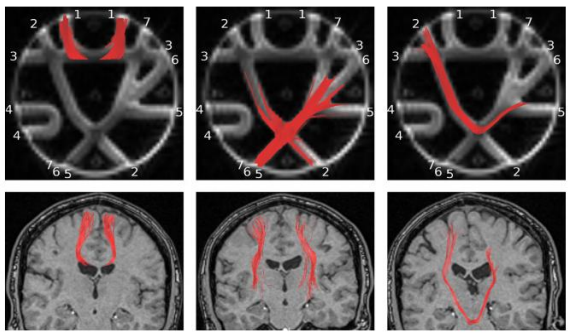

Figure 4.3 :*No connections (NC) due to many collisions with the tracking mask or angular constraints not met, both causing the tracking process to finish prematurely on the FiberCup and the real data analogies.[80]*

IC are reported in %. According to tractometer team survey with clinicians, these are the most problematic streamlines as they ‘‘appear plausible’’ (because for example they connect gray matter regions) but are in fact non-existent from a priori anatomical knowledge.

d) No Connections (NC): streamlines that do not connect two ROIs. Depending on how fiber tracking handles stopping criteria, these streamlines stop prematurely either due to angular constraints or, most often, due to hitting the boundaries of the tracking mask, as illustrated in Figure.4.3.

e) Valid Bundles (VB): bundles connecting expected ROIs. Figure. 4.4 (left) shows the valid bundles. VB is reported in bundle counts, from 0 to 7 for the FiberCup. For example, in Figure. 4.1, VB = 7.

f) Invalid Bundles (IB): bundle connecting unexpected ROIs. As VB, IB is reported in bundle counts and is similar to IC, but at the bundle scale. For example, this is shown in Figure. 4.2, where bundles 1, 3 are mismatched. However, note that they ‘‘look anatomically plausible’’, had we not known the ground truth. In theory, there are a total of 39 possible IB.

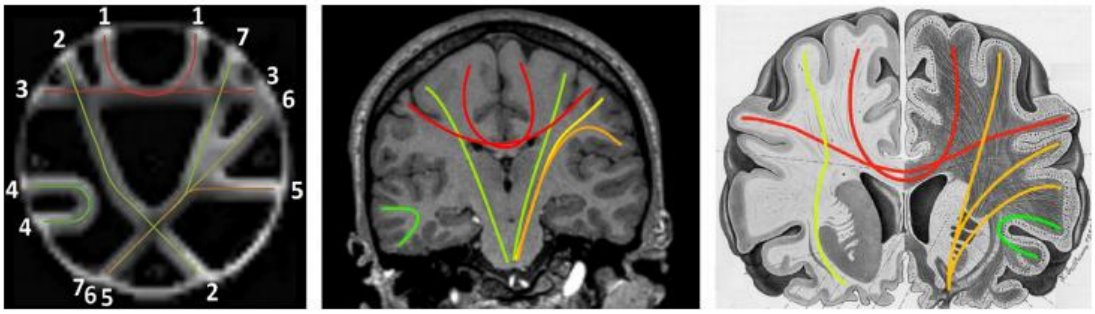

Figure 4.4:*FiberCup mimicking a coronal slice of the brain with typical short ‘U’ fibers (bundle 4), larger ‘U’ fibers mimicking the corpus callosum (bundle 1), left-to-right hemisphere commissural projections (bundle 3) and fanning bundles mimicking the corticospinal tract (bundles 2, 5, 6 and7)[80].*

4.3 Phantom Data preparation:

4.3.1 Phantom Data :

The data used in the evaluation is the same data used in the 2013 International Symposium on BIOMEDICAL IMAGING challenge[81]. The data is sampled with 64 direction and b=3000 s/mm^2 ,we have used three datasets with three different SNR[10] values 10,20 and 30 the files are in nifti format (.nii.gz) and b-vector and b-value files ,with a white matter mask, and seed mask interface.

4.3.2 Tractography evaluation pipeline:

In order to make the evaluation using tractometer we have to do some preprocessing and creating a trackvis (.trk) files, after that we submit the .trk files to the tractometer team at Sherbrooke Connectivity Imaging Lab .To get the results the pipeline for evaluating the results is in Figure 4.5.

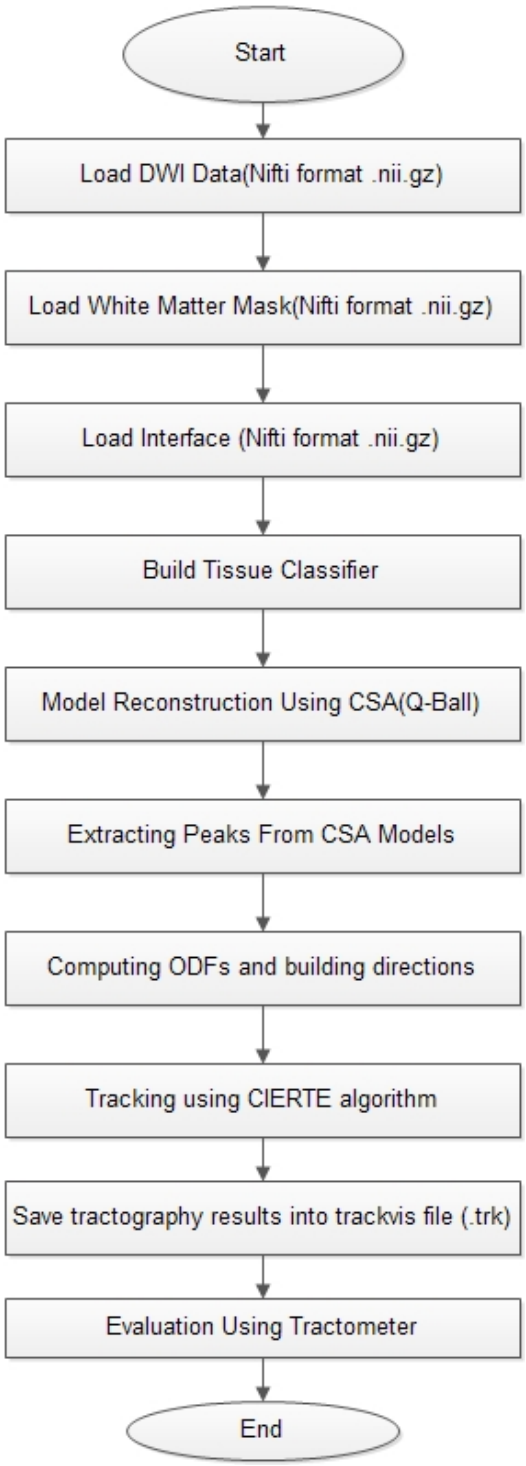

Figure 4.5: *Tractography Evaluation pipeline*

4.4 Tractometer Results:

We applied CIERTE algorithms to three different state of the art Tractography algorithms tow deterministic algorithms and one probabilistic algorithm these algorithms are implemented into the library dipy [82] we re-implement the CIERTE algorithm and make it compatible with Eudx [1], Deterministic maximum direction getter and Probabilistic maximum direction getter algorithms[1].

In order to make a good study on the algorithms we apply CIRETE algorithm using different SNR values, we change the number of seeds per voxel (NPV) and finally choose different step sizes (SS) 0.2, 0.3, 0.4 and 0.5. In order to obtain the tractometer results we generate the trackvis results (.trk) files and send them to Sherbrooke Connectivity Imaging Lab (SCIL).

4.4.1 Deterministic Results:

We have implemented a deterministic tractography algorithm CIERTE-Det. After data preprocessing we use CIERTE-Det, which is a modified version of Dipy-Eudx algorithm, we implement it in order to make comparative study on the algorithms and the improvements. The tractometer results for the three deterministic algorithms CIERTE-Det , Dipy-Eudx and Dipy-MX are shown in table 4.1.

Table 4.2: *Comparison between CIERTE-Det , Dipy-Eudx and Dipy-Mx algorithms using three different SNR 10,20,30 and step size 0.2,0.3,0.4 and NPV 50 and 20.*

Algorithm	SNR	NPV	SS	ABC %	IB	IC%	NC%	VB	VC%	CSR	VCCR
CIERTE-Det	10	50	0.4	39.7	36	8.7	69.1	26	22.2	30.9	71.8
CIERTE- Det	10	50	0.3	40.2	38	9.5	67.4	26	23.1	32.6	71.0
CIERTE- Det	10	50	0.2	40.6	38	9.8	65.1	26	25.0	34.9	71.8
CIERTE- Det	10	20	0.5	35.1	34	8.1	71.6	26	20.4	28.4	71.7
CIERTE- Det	20	20	0.5	37.4	27	8.1	70.0	26	22.0	30.0	73.1
CIERTE- Det	30	20	0.5	36.0	24	7.2	69.4	25	23.4	30.6	76.5
Dipy-Eudx	10	50	0.2	42.6	40	11.6	60.8	26	27.6	39.2	70.4
Dipy-Mx	30	50	0.2	51.1	43	18.5	26.2	26	55.3	73.8	74.9

VCCR = VC/(VC+IC) , CSR = VC + IC

As we can see clearly from table 4.1 when we compare CIERTE deterministic algorithm with dipy eudx deterministic algorithm. CIERTE algorithm give us less invalid

bundles (IB) and less invalid connections compared to Dipy-Eudx algorithm for all step sizes and all SNR values. Although CIERTE algorithm give less valid connections rather then Eudx, but this is not a big difference if compare strictly the one with 0.2 step size to Eudx . We get 26 valid bundles except for SNR 30 when we have 25 valid bundles, we have also good valid connection-to-connection ratio (VCCR), which is more than 71% for all CIERTE results.

Average bundle coverage (ABC) is small for CIERTE with a maximum of 40.2 compared to Eudx with 42.6.

As we decrease the step size CIERTE algorithm, get better ABC, value increase going from 35.1 up to 40.6. For valid connection (VC) reducing the step size maximize the valid connectivity but in the other side increase both invalid bundle (IB) and invalid connections (IC), but if we compare VCCR we almost get the same 71.8. Since the best valid connection is 25% for 0.2 step size, we can see clearly that taking 0.2 as step size give us the best results.

Another factor that we can see is the signal to noise ratio (SNR), as we increase SNR value ABC increases and we get the lowest IC 7.2% .Also the valid connections increase as SNR increase, we get the maximum VCCR 76.5%, although the step size used is 0.5 and NPV is 20 comparing that to Dipy-Mx we have less invalid bundles and invalid connection. In CIERTE-Det for SNR 30 although VC and VB is high in Dipy-Mx but VCCR is better for CIERTE-Det this result lead us to conclude.

CIERTE algorithm help in reducing the invalidity of bundles and connections, which is a major problem in tracking algorithms because having less invalidity, is better than having more valid bundles at the cost of invalid ones. Choosing a good step size reduce the error more ,but changing the step size in our study yield small difference. If we compare CIERTE algorithm using 0.4 as step size and Eudx with 0.2 as step size ,we can see clearly that CIERTE algorithm has less invalidity in bundles and in connections compared to Eudx, the difference between the two algorithms is that Eudx will take 2 steps compare to CIERTE algorithm which will take one step with a second order approximation, which make the tow algorithms have almost the same time complexity, but as we have seen in chapter 3 reducing the step size by the factor of tow will create tow tracking points in memory which increase the memory usage ,in this case we prefer to use CIERTE algorithm because, if we want to visualize billions of neurons reducing the step size cost us more hardware hence more

money, also having a good SNR play a role in reducing the error which we have seen clearly in our study.

4.4.2 Probabilistic Results:

We have implemented a tractography algorithm CIERTE-Prob which an application of CIERTE algorithm on the Probabilistic Maximum Direction Getter used by dipy library.

After data preprocessing which uses CSD model as reconstruction technique, we use CIERTE-Prob The tractometer results for CIERTE-Prob and dipy Probabilistic Maximum Direction Getter are shown in table 4.2

Table 4.3 :*Comparison between CIERTE-Prob and Maximum direction getter(Dipy-Prob) algorithms using step size (SS) 0.2,0.3,0.4 and NPV 50 and 20*

Algorithm	SNR	NPV	SS	ABC %	IB	IC%	NC%	VB	VC%	CSR	VCCR
CIERTE-Prob	10	50	0.4	49.6	123	14.4	70.6	26	15.0	29.4	51.0
CIERTE-Prob	10	50	0.3	31.6	85	17.4	66.7	16	15.9	33.3	47.7
CIERTE-Prob	10	50	0.2	50.2	136	17.0	66.6	26	16.4	33.4	49.1
Dipy-Prob	10	50	0.2	46.4	100	11.1	77.8	25	11.1	22.2	49.9

As we can see from table 4.2 which is a comparison between CIERTE probabilistic algorithm with dipy probabilistic maximum direction getter algorithms. The number of invalid bundles (IB) varies from 85 to 136 for CIERTE and 100 for dipy probabilistic algorithm, comparing CIERTE with 0.2 step size to dipy probabilistic. CIERTE have more ABC 50.2 compared to dipy and have more invalid bundles rather than dipy, but higher valid bundles and valid connections (VC) compared to dipy and almost the same VCCR, with step size, 0.3 we have 85 IB but only 16 VB. As we can see for probabilistic results we have good ABC value, since the probabilistic algorithm produce more directions than deterministic algorithms, we have also more invalid connections and valid connections compared to deterministic algorithms. Although we have, good results compared to dipy probabilistic algorithms but overall, probabilistic algorithms are less accurate and difficult to compare due to the probability of many directions.

4.5 Visualization of phantom results:

The phantom data used in the evaluation is from the International Symposium on BIOMEDICAL IMAGING 2013 challenge, the data is a 4 dimension matrix with (50, 50, 50, 60) 3D data + weighting, from the weighting data we get the Fiber orientation distributions (FOD) using constant solid angle (csa) or Q-ball

Figure 4.6 shows us 3 different slices from axial, coronal and sagittal, and how we get the FOD directions from each slice the FOD images are used for getting the tracking directions

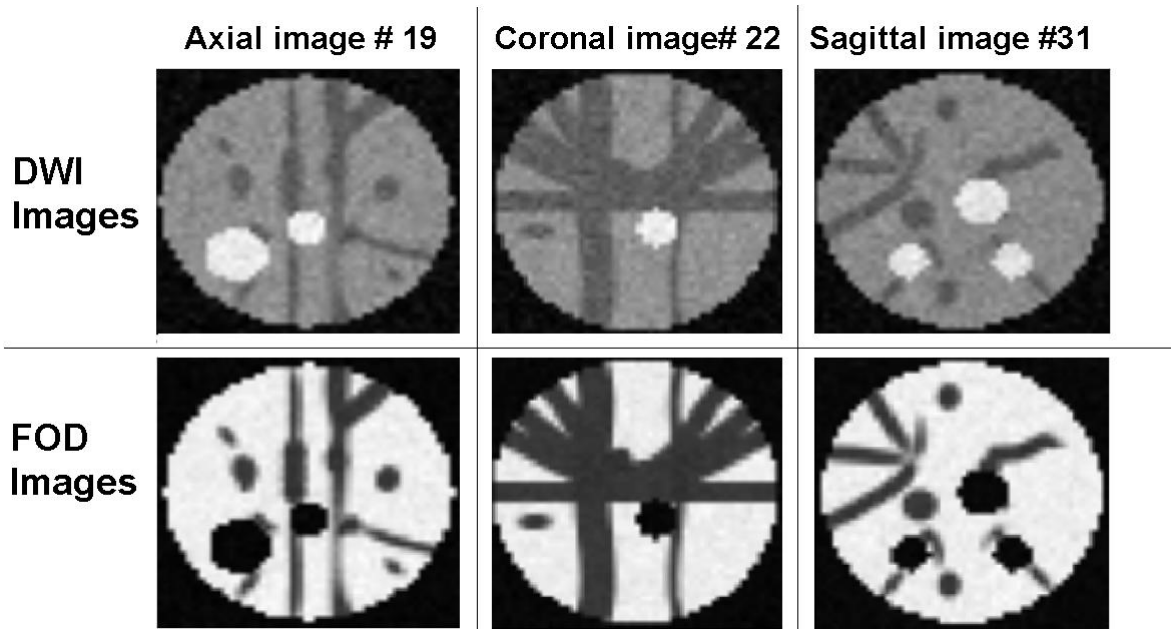

Figure 4.6 : *some DWI images (axial #19,coronal #22 and sagittal #31) used for tractography evaluation and their Fiber orientation direction images (FOD)*

The CIERTE algorithm is implemented in our software DIVIZ [74], which is a software we created in our LICENCE degree to visualize and reconstruct the fiber tractography of the brain, using DIVIZ for visualization give us the results we want as illustrated in Figure 4.7

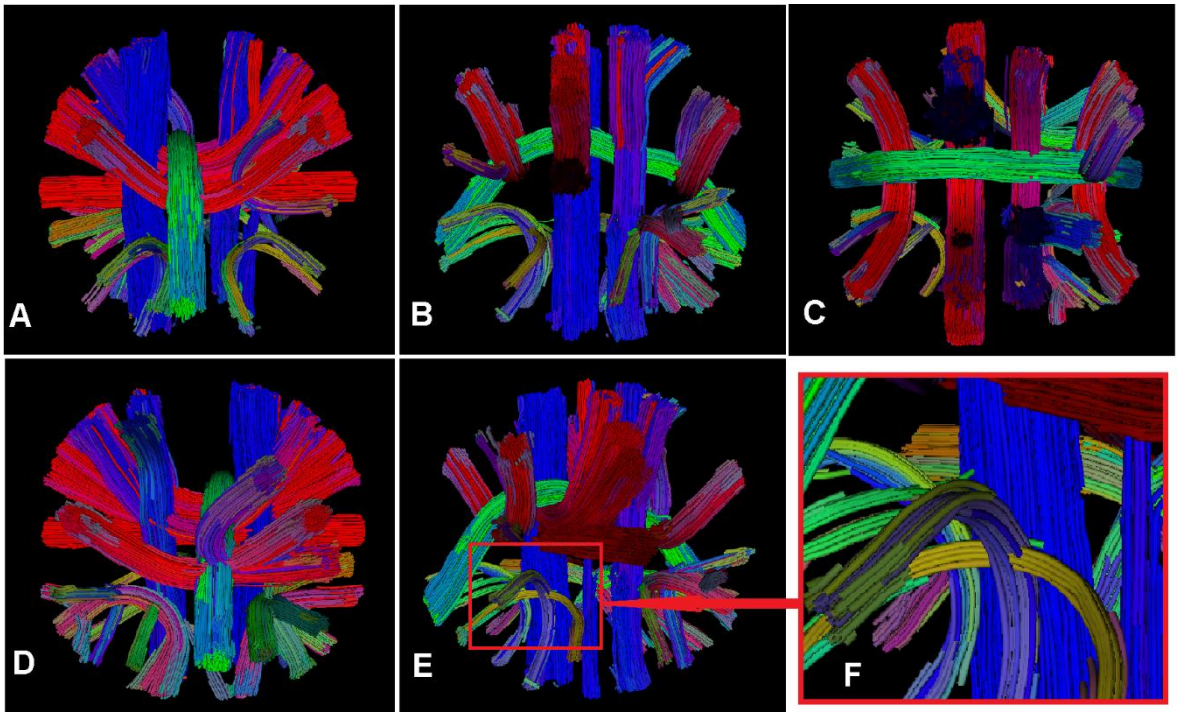

Figure 4.7:*visualization of CIERTE tractography results of the phantom data used to evaluate the tractometer results ,images A,B,C,D,E,F are phantom tractography visualization from different points of view ,images E and F illustrate some crossing fibers.*

As we can see clearly from Figure 4.7 the results we get using CIERTE algorithm are good results comparing to the input data, we can see clearly from images E and F in Figure 4.7 CIERTE algorithm solve the issue of crossing fibers.

4.6 Summary:

From what we have seen, CIERTE algorithm works well for deterministic tractography rather than probabilistic tractography, we have focused our stud improving the tracking algorithm and make a comparative study with different tracking criterion like step size number of seeds per voxels but although the valid connections need more accuracy many things need to be taken into consideration in order to produce the best tracking results one of these criteria is SNR which is a good factor as we have seen in deterministic algorithms ,this last helps us increase the valid connections and decrease the invalid ones ,we have seen also how choosing a good tracking algorithm help reducing uncertainty ,this uncertainty in our algorithm can be improved more with a good acquisitions and improving in the reconstruction techniques.

CONCLUSION:

Streamline tractography algorithms have been used with many dMRI reconstruction methods and because the simplicity of this algorithms and the well understanding of them let us develop the CIERTE algorithm. These algorithms are susceptible to three main sources of errors [83]. First, DWI is susceptible to imaging noise, which may cause a poor estimation of the dominant diffusion directions used in streamline tractography.

Secondly, the microscopic anatomy of WM is bound to be more complex than what can be represented by the fiber reconstruction model. As such, streamline tractography is subject to modeling errors. This is especially true for tractography algorithms using the diffusion tensor model, which cannot resolve multiple fiber orientations inside one voxel. Note that the uncertainty suddenly increases as soon as the trajectories enter regions of crossing fibers.

Finally, streamline tractography is subject to integration errors. It is important to realize that all these errors will accumulate along the streamline. We had focus our study on the effect of integration error and how this last effect the streamline more than any other parameter, also we have seen the difference between reconstruction models and there effects, and the effect of changing SNR. Note that, for large SNR, the variability in the fiber orientation is low, but the fiber orientations can become unreliable at low SNR.

We validate the CIERTE tractography results using the Tractometer evaluation system, which give credibility to our new proposed algorithm hoping to make it general in all tractography algorithms.

We have seen also how CIERTE can be used to handle big data, and how the number of seed points can have a major effect on losing some fibers. CIERTE allows you to choose the low threshold values for anisotropy measures, which defer from one reconstruction method to another. From the results, we have seen we could say that CIERTE try to solve some of the known deterministic problems especially when speed and accuracy are needed.

References :

[1] EleftheriosGaryfallidis, *"Towards an Accurate Brain Tractography"*, University of Cambridge, May (2012).

[2] S. Mori, B. J. Crain, V. P. Chacko, and P. C. van Zijl, "*Three-dimensional tracking of axonal projections in the brain by magnetic resonance imaging*" Ann Neurol, vol. 45, no. 2, pp. 265–9, (1999).

[3] P. J. Basser, S. Pajevic, C. Pierpaoli, J. Duda, and A. Aldroubi, "*In vivo fiber tractography using DT-MRI data*" MagnReson Med, vol. 44, no. 4, pp. 625–32, (2000).

[4] Jean Philibert, "One *and a Half Century of Diffusion: Fick, Einstein, Before and Beyond*", Extended version of Jean Philibert's contribution to the Proceedings of Diffusion Fundamentals I, Leipzig, 2005 (2006).

[5] Patric Hagmann, "*From Diffusion MRI to BrainConnectomics*", Ecole Polytechnique Fédérale De Lausanne, Thèse POUR L'OBTENTION DU GRADE DE DOCTEUR `ES SCIENCES, N3230 (2005).

[6] Fick A, "*On Liquid Diffusion*", London, Edinburgh, and Dublin Philosophical Magazine and Journal of Science, Vol. X (1855) 30-39.Abstracted by the author from the German original: Uber Diffusion, Poggendorff'sAnnalen der Physik und Chemie, (1855) 59-86.

[7] Bram Stieltjes, Romuald M. Brunner, Klaus H. Fritzsche and Frederik B. Laun, *"Diffusion Tensor Imaging Introduction and Atlas",* Springer (2013).

[8] PatricHagmann et al, "*Understanding Diffusion MR Imaging Techniques: From Scalar Diffusion-weighted Imaging to Diffusion Tensor Imaging and Beyond*", **(**October 2006).

[9] Jan Hrabe et al, *"Principles and limitations of NMR diffusion measurements",* journal of US National Library of Medicine of National Institutes of Health, (2007).

[10] Yung-Chin Hsu / Wen-Yih Isaac Tseng "*Slides_hbm_diffusion*". Center for Optoelectronic Medicine, National Taiwan University Hospital.

[11] Olaf Dietrich et al, *"Measurement of Signal-to-Noise Ratios in MR Images: Influence of Multichannel Coils, Parallel Imaging, and Reconstruction Filters"*, journal from Magnetic Resonance Imaging (2007).

[12]Jeurissen, *"Improved analysis of brain connectivity using high angular resolution diffusion MRI",* PH.D thesis, (2012).

[13] Andrew L. Alexander, JeeEun Lee, Mariana Lazar, and Aaron S. Field, *"Diffusion Tensor Imaging of the Brain"*, Neurotherapeutics, Vol. 4, No. 3, (2007).

[14] V. Wedeen, P. Hagmann, W. Tseng, T. Reese, and R. Weisskoff, "*Mapping complex tissue architecture with diffusion spectrum magnetic resonance imaging* " Magnetic Resonance in Medicine, vol. 54, no. 6, pp. 1377–1386, (2005).

[15] D. Tuch, *"Q-ball imaging"* , Magnetic Resonance in Medicine, vol. 52, no. 6, pp. 1358–1372, (2004).

[16] D. Tuch, "*Diffusion MRI of complex tissue structure"*. PhD thesis, Massachusetts Institute of Technology, Division of Health Sciences and Technology, (2002).

[17] Descoteaux, M., Deriche, R., Bihan, D. L., Mangin, J.-F., and Poupon, C. (2011). "*Multiple q-shell diffusion propagator imaging*" .Med. Image Anal.15, 603–621.doi: 10.1016/j.media.2010.07.001.

[18] Tournier, J.-D., Calamante, F., Gadian, D., and Connelly, A. (2004). "*Direct estimation of the fiber orientation density function from diffusion-weighted MRI data using spherical deconvolution*".Neuroimage23, 1176–1185. doi:10.1016/j.neuroimage.2004.07.037.

[19] Tournier, J.-D., Calamante, F., and Connelly, A. (2007). "*Robust determination of the fibre orientation distribution in diffusion mri: non-negativity constrained super-resolved spherical deconvolution*". Neuroimage35, 1459–1472.doi: 10.1016/j.neuroimage.2007.02.016.

[20] T. E. Conturo, N. F. Lori, T. S. Cull, E. Akbudak, A. Z. Snyder, J. S. Shimony, R. C. McKinstry, H. Burton, and M. E. Raichle, "*Tracking neuronal fiber pathways in the living human brain*" ProcNatlAcadSci U S A, vol. 96, no. 18, pp. 10422–7, (1999).

[21] P. J. Basser, S. Pajevic, C. Pierpaoli, J. Duda, and A. Aldroubi, "*In vivo fiber tractography using DT-MRI data*" MagnReson Med, vol. 44, no. 4, pp. 625–32, (2000).

[22] D. Tuch, "*Diffusion MRI of complex tissue structure"*. PhD thesis, Massachusetts Institute of Technology, Division of Health Sciences and Technology, (2002).

[23] V. Wedeen, P. Hagmann, W. Tseng, T. Reese, and R. Weisskoff, "*Mapping complex tissue architecture with diffusion spectrum magnetic resonance imaging* " Magnetic Resonance in Medicine, vol. 54, no. 6, pp. 1377–1386, (2005).

[24] J. Tournier, F. Calamante, D. Gadian, A. Connelly, et al., "*Direct estimation of the fiber orientation density function from diffusion-weighted mri data using spherical deconvolution*" NeuroImage, vol. 23, no. 3, pp. 1176–1185, (2004).

[25] V. J. Wedeen, R. P. Wang, J. D. Schmahmann, T. Benner, W. Y.Tseng, G. Dai, D. N. Pandya, P. Hagmann, H. D'Arceuil, and A. J.de Crespigny, "*Diffusion spectrum magnetic resonance imaging (DSI) tractography of crossing fibers*" Neuroimage, vol. 41, no. 4, pp. 1267–77, (2008).

[26] Y. Chao, J. Chen, K. Cho, C. Yeh, K. Chou, and C. Lin, "*A multiple streamline approach to high angular resolution diffusion tractography*" Medical engineering and physics, vol. 30, no. 8, pp. 989–996, (2008).

[27] M. Descoteaux, R. Deriche, T. R. Knösche, and A. Anwander, "*A Deterministic and probabilistic tractography based on complex fibre orientation distributions*" IEEE transactions on medical imaging, vol. 28, pp. 269–86, Feb. (2009).

[28] M. Lazar, D. M. Weinstein, J. S. Tsuruda, K. M. Hasan, K. Arfanakis, M. E. Meyerand, B. Badie, H. A. Rowley, V. Haughton, A. Field, and A. L. Alexander, "*White matter tractography using diffusion tensor deflection*" Hum Brain Mapp, vol. 18, no. 4, pp. 306–21, (2003).

[29] G. J. M. Parker, H. A. Haroon, and C. A. M. Wheeler-Kingshott, "*A framework for a streamline-based probabilistic index of connectivity (PICo) using a structural interpretation of MRI diffusion measurements*" Journal of Magnetic Resonance Imaging, vol. 18, no. 2, pp. 242–54, (2003).

[30] T. E. J. Behrens, M. W. Woolrich, M. Jenkinson, H. Johansen-Berg, R. G. Nunes, S. Clare, P. M. Matthews, J. M. Brady, and S. M. Smith, "*Characterization and propagation of uncertainty in diffusion-weighted {MR} imaging*" Magnetic Resonance in Medicine, vol. 50, pp. 1077–1088, (2003).

[31] T. Behrens, H. Johansen-Berg, S. Jbabdi, M. Rushworth, and M. Woolrich, "*Probabilistic diffusion tractography with multiple fibre orientations: What can we gain?*" NeuroImage, vol. 34, no. 1, pp. 144–155, (2007).

[32] T. Hosey, G. Williams, and R. Ansorge, "*Inference of multiple fiber orientations in high angular resolution diffusion imaging*" Magnetic Resonance in Medicine, vol. 54, no. 6, pp. 1480–1489, (2005).

[33] O. Friman, G. Farneback, and C. Westin, "*A Bayesian approach for stochastic white matter tractography*" Medical Imaging, IEEE Transactions on, vol. 25, no. 8, pp. 965–978, (2006).

[34] F. Zhang, E. Hancock, C. Goodlett, and G. Gerig, "*Probabilistic white matter fiber tracking using particle filtering and von mises-fisher sampling*" Medical image analysis, vol. 13, no. 1, pp. 5–18, (2009).

[35] S. Pajevic and P. Basser, "*Parametric and non-parametric statistical analysis of DT-MRI data*" Journal of Magnetic Resonance, vol. 161, no. 1, pp. 1–14, (2003).

[36] M. Lazar and A. Alexander, "*Bootstrap white matter tractography (BOOT-TRAC)*" NeuroImage, vol. 24, no. 2, pp. 524–532, (2005).

[37] R. O'Gorman and D. Jones, "*Just how much data need to be collected for reliable bootstrap DT-MRI?*," Magnetic resonance in medicine, vol. 56, no. 4, pp. 884–890, (2006).

[38] H. Johansen-Berg and T. E. J. Behrens, eds., "*Diffusion MRI"*. Academic Press, 2009.

[39] S. Jbabdi, M. Woolrich, J. Andersson, and T. Behrens, "*A Bayesian framework for global tractography*" Neuroimage, vol. 37, no. 1, pp. 116–129, (2007).

[40] G. Parker, C. Wheeler-Kingshott, and G. Barker, "*Estimating distributed anatomical connectivity using fast marching methods and diffusion tensor imaging*" Medical Imaging, IEEE Transactions on, vol. 21, no. 5, pp. 505–512, (2002).

[41] J. Tournier, F. Calamante, D. Gadian, A. Connelly, et al., "*Diffusion-weighted magnetic resonance imaging fibre tracking using a front evolution algorithm*" NeuroImage, vol. 20, no. 1, pp. 276–288, (2003).

[42] J. Campbell, K. Siddiqi, V. Rymar, A. Sadikot, and G. Pike, "*Flow-based fiber tracking with diffusion tensor and q-ball data: validation and comparison to principal diffusion direction techniques*" NeuroImage, vol. 27, no. 4, pp. 725–736, (2005).

[43] P. Fletcher, R. Tao, W. Jeong, and R. Whitaker, "*A volumetric approach to quantifying region-to-region white matter connectivity in diffusion tensor MRI*" in Information Processing in Medical Imaging, pp. 346–358, Springer, (2007).

[44] X. Gigandet; "*Global brain connectivity analysis by diffusion MR tractography: algorithms, validation and applications"*. PhD thesis, ÉcolePolytechniqueFédérale de Lausanne, (2009).

[45] Y. Iturria-Medina, E. Canales-Rodríguez, L. Melie-García, P. Valdés-Hernández, E. Martínez-Montes, Y. Alemán-Gómez, and J. M.Sánchez-Bornot, "*Characterizing brain anatomical connections using diffusion weighted MRI and graph theory*" Neuroimage, vol. 36,no. 3, pp. 645–660, (2007).

[46] A. Zalesky, "*DT-MRI fiber tracking: a shortest paths approach*" Medical Imaging, IEEE Transactions on, vol. 27, no. 10, pp. 1458–1471, (2008).

[47] S. Lifshits, A. Tamir, and Y. Assaf, "*Combinatorial fiber-tracking of the human brain*" NeuroImage, vol. 48, no. 3, pp. 532–540, (2009).

[48] P. Fillard, C. Poupon, and J. Mangin, "*A novel global tractography algorithm based on an adaptive spin glass model*" Medical Image Computing and Computer-Assisted Intervention, pp. 927–934, (2009).

[49] S. Sotiropoulos, L. Bai, P. Morgan, C. Constantinescu, and C. Tench, "*Brain tractography using Q-ball imaging and graph theory: Improved connectivities through fibre crossings via a model-based approach*" NeuroImage, vol. 49, no. 3, pp. 2444–2456, (2010).

[50] B. Kreher, I. Mader, and V. Kiselev, "*Gibbs tracking: a novel approach for the reconstruction of neuronal pathways*" Magnetic Resonance in Medicine, vol. 60, no. 4, pp. 953–963, (2008).

[51] B.W.Kreher, I. Mader, and V. G. Kiselev, "*Gibbs tracking: A novel approach for the reconstruction of neuronal pathways*" Proc. Intl. Soc. Mag. Reson. Med., vol. 16, p. 425, (2008).

[52] M. Reisert, I. Mader, C. Anastasopoulos, M. Weigel, S. Schnell, and V. Kiselev, "*Global fiber reconstruction becomes practica*l" Neuroimage, vol. 54, no. 2, pp. 955–962, (2011).

[53] M. Lazar and A. Alexander, "*White matter tractography using random vector (RAVE) perturbation*" in Proceedings of ISMRM Annual Meeting, Honolulu, (2002).

[54] P. Fillard, C. Poupon, and J. Mangin, "*Spin Tracking: A Novel Global Tractography Algorithm*" NeuroImage, vol. 47, pp. S127–S127, (2009).

[55] A. Sherbondy, M. Rowe, and D. Alexander, "*Microtrack: An algorithm for concurrent projectome and microstructure estimation*" Medical Image Computing and Computer-Assisted Intervention, pp. 183–190, (2010).

[56] D. Alexander, P. Hubbard, M. Hall, E. Moore, M. Ptito, G. Parker, and T. Dyrby, "*Orientationally invariant indices of axon diameter and density from diffusion MRI*" NeuroImage, vol. 52, no. 4, pp. 1374–1389, (2010).

[57] P. Batchelor, D. Hill, D. Atkinson, and F. Calamante, "*Study of connectivity in the brain using the full diffusion tensor from MRI*" in Information Processing in Medical Imaging, pp. 121–133, Springer, (2001).

[58] N. Kang, J. Zhang, E. Carlson, and D. Gembris, "*White matter fiber tractography via anisotropic diffusion simulation in the human brain*" Medical Imaging, IEEE Transactions on, vol. 24, no. 9, pp. 1127– 1137, (2005).

[59] N. Hageman, A. Toga, K. Narr, and D. Shattuck, "*A diffusion tensor imaging tractography algorithm based on navier–stokes fluid mechanics*" Medical Imaging, IEEE Transactions on, vol. 28, no. 3, pp. 348–360, (2009).

[60] P. Hagmann, J. Thiran, L. Jonasson, P. Vandergheynst, S. Clarke, P. Maeder, and R. Meuli, "*DTI mapping of human brain connectivity: statistical fibre tracking and virtual dissection*" Neuroimage, vol. 19, no. 3, pp. 545–554, (2003).

[61] Garyfallidis E, Brett M, Amirbekian B, Rokem A, Van_der_walt S, Descoteaux M and Nimmo-smith I(2014) "*Dipy, a library for the analysis of diffusion MRI data*". Front. Neuroinform. (2014).

[62] F. Yeh, V. Wedeen, and W. Tseng, "Estimation of fiber orientation and spin density distribution by diffusion deconvolution," Neuroimage, vol. 55, no. 3, pp. 1054–1062, (2011).

[63] Components of the Human Connectome Project Diffusion Tractography: http://www.humanconnectome.org/about/project/tractography.html

[64] Cherifi, D ;Chellouche, A. ; Ouakli, A.A. ; Benamara, Y. and Deriche, R. “Tensor estimation and visualization using dMRI” IEEE Systems, Signal Processing and their Applications (WoSSPA), 8th International Workshop on (2013) DOI: 10.1109/WoSSPA.2013.6602337

[65] Euler Method from Wikipedia:

http://en.wikipedia.org/wiki/Euler_method

[66] Error in Euler Method:

http://www.math.unl.edu/~gledder1/Math447/EulerError

[67] Wikipedia trapezoidal rule:
http://en.wikipedia.org/wiki/Trapezoidal_rule_%28differential_equations%29

[68] Heun’s Method:

http://en.wikipedia.org/wiki/Heun%27s_method

[69] Improved Euler:

http://www.math.ubc.ca/~israel/m215/impeuler/impeuler.html

[70] Numerical Methods for First Order Equations :

http://www.math.poly.edu/courses/ma2132/Notes/MA2132NumericalMethods.pdf

[71] Runge–Kutta methods:
http://en.wikipedia.org/wiki/Runge%E2%80%93Kutta_methods

[72] S.Mori and P.C.M.VanZijl. "*Fiber tracking: principles and strategies-a technical review"*. NMR in Biomedicine, 15(7-8):468–480, (2002).

[73] Stanford hardi dataset:
https://stacks.stanford.edu/file/druid:yx282xq2090/dwi.nii.gzhttps://stacks.stanford.edu/file/druid:yx282xq2090/dwi.bvalshttps://stacks.stanford.edu/file/druid:yx282xq2090/dwi.bvecs

[74] BOUDJADA Messaoud, MORSLI Abdelatif, DAHOUMAN Brahim ,Supervisor Dr CHERIFI Dalila*,"Software Development For Brain Fibers Tractography",* LICENCE report , Institute of Electrical and Electronic Engineering ,University M'Hamed BOUGARA –BOUMERDES, (2014).

[75] Tuch DS, Weisskoff RM, Belliveau JW, Wedeen VJ. *"High angular resolution diffusion imaging of the human brain"*. Proceedings of the 7th Annual Meeting of the ISMRM, Philadelphia (1999)..

[76] Berman JI, Berger MS, Mukherjee P, Henry RG. *"Diffusion-tensor imaging-guided tracking of fibers of the pyramidal tract combined with intraoperative cortical stimulation mapping in patients with gliomas"*. J Neurosurg (2004) ;101:66-72.

[77] Wu J, Zhou L, Tang W, Mao Y, Hu J, Song Y, Hong X, Du G, 2007. *"Clinical evaluation and follow-up outcome of diffusion tensor imaging-based functional neuronavigation: a prospective, controlled study in patients with gliomas involving pyramidal tracts".* Neurosurgery (2007) 61, 935–949.

[78] Spena G, Nava A.,Cassini F, Pepoli A, Bruno M, D'Agata F, Caud F, Sacco K, Duca S, Barletta L, Versari P. *"Preoperative and intra-operative brain mapping for the resection of eloquent- area tumors: a prospective analysis of methodology, correlation, and usefulness based on clinical outcomes"*. ActaNeurochirurgica (2010) 152, 1835–1846.

[79] Fillard P, Descoteaux M, Goh A, Gouttard S, Jeurissen B, Malcolm J, Ramirez Manzanares A, Reisert M, Sakaie K, Tensaouti F, Yo T, coisMangi, J.F, Poupon C, *"Quantitative evaluation of 10 tractography algorithms on a realistic diffusion mr phantom"*. NeuroImage(2011). 56, 220–234.

[80] Marc-Alexandre Côté, Gabriel Girard, Arnaud Boré, EleftheriosGaryfallidis, Jean-Christophe Houde, MaximeDescoteaux. *"Tractometer:Towards validation of tractography pipelines"*, (2013)

[81] http://www.biomedicalimaging.org/2013/program/isbi-challenges/

[82] http://nipy.org/dipy/

[83] T.E.J.Behrens and S.Jbabdi. *"MR diffusion tractography in Diffusion MRI: from quantitative measurement to in vivo"* neuroanatomy, pages 333–351. Academic Press, (2009).